Spintronic Devices for High-density Memory and Neuromorphic Computing – A Review

BingJin Chen[a,1], Minggang Zeng[2], Khoong Hong Khoo[1], Shunsuke Fukami[3,4], Sai Li[5], Weisheng Zhao[6], Stuart S. P. Parkin[7], S.N. Piramanayagam[a,8] and Sze Ter Lim[a,9]

[1]*Institute of High Performance Computing (IHPC), Agency for Science, Technology and Research (A*STAR), 1 Fusionopolis Way, #16-16 Connexis, Singapore 138632, Republic of Singapore*

[2]*Institute for Infocomm Research (I2R), Agency for Science, Technology and Research (A*STAR), 1 Fusionopolis Way, #21-01 Connexis, Singapore 138632*

[3]*Research Institute of Electrical Communication, Tohoku University, Sendai 980-8577, Japan*

[4]*Center for Science and Innovation in Spintronics, Tohoku University, Sendai 980-8577, Japan*

[5]*Fert Beijing Institute, School of Computer Science and Engineering, Beihang University, Beijing, China*

[6]*Fert Beijing Institute, School of Integrated Circuit Science and Engineering, Beihang University, Beijing, China*

[7]*Max Planck Institute of Microstructure Physics, Weinberg 2, 06120 Halle, Germany*

[8]*School of Physical and Mathematical Sciences, Nanyang Technological University, Singapore 637371*

[9]*Institute of Materials Research and Engineering (IMRE), Agency for Science, Technology and Research (A*STAR), 2 Fusionopolis Way, #08-03, Innovis, Singapore 138634*

[a]Corresponding authors: email: Chen_BingJin@ihpc.a-star.edu.sg; prem@ntu.edu.sg; Lim_Sze_Ter@imre.a-star.edu.sg

ABSTRACT

Spintronics is a growing research field that is focused on exploring materials and devices that take advantage of the electron's "spin" to go beyond charge based devices. The most impactful spintronic device to date is a highly sensitive magnetic field sensor, the spin-valve, that allowed for a 10,000-fold increase in the storage capacity of hard disk drives since it was first introduced in a magnetic recording read head in 1997. In about 2007 the original spin-valve that was based on spin-dependent scattering in metallic magnetic/non-magnetic interfaces evolved to a closely related device in which the essential physics changed to that of spin-dependent tunneling across ultra-thin insulating layers placed between magnetic electrodes, but the basic spin-engineered structure remained largely unchanged. These latter structures were proposed in 1995 as potential memory elements for a magnetic random-access memory (MRAM) and the first demonstration of this possibility was made in 1999. It was only recently (about 2019) that MRAM became a mainstream foundry technology.

Compared with most conventional charge based electronic devices, spintronic devices have the advantage of non-volatility, low-power consumption, and scalability to smaller dimensions. For these reasons spintronic devices are highly attractive for next-generation information memory-storage and are promising for advanced applications such as in-memory computing. Furthermore, spintronics allows for a unique high capacity, non-volatile, solid-state memory-storage device that relies on devices that can store multiple digital bits in the form of a series of chiral domain walls that are moved at high-speed using nanosecond long current pulses along magnetic nanowires. These devices also enable synaptic functionalities in neuromorphic computing and are therefore potential hardware candidates for artificial intelligence.

In this review article, recent advances in multi-state spintronic devices are discussed. The review starts with an introduction followed by a discussion on using domain-walls for achieving multiple states for memory and neuromorphic computing. In the next section, achieving multiple levels based on domain nucleation are discussed. Subsequent discussions review the use of magnetic pillars, and other schemes for achieving high-density memory. The prospects of spintronic devices in neuromorphic computing for artificial intelligence (AI) are also presented.

Contents

I. INTRODUCTION

The invention of the computer and its variants, such as smartphones, has enormously impacted and augmented the human way of life. For the past 40 years, computers themselves have continuously evolved according to the Moore's law evolution of the number of transistors in a single silicon chip that has allowed for ever-increasing computing power. At the same time, the main technology used for storing digital data, the magnetic hard disk drive (HDD), has also continuously evolved with ever-increasing storage capacity per disk. These evolutions have required, at times, discontinuous changes in the sub-component technologies, as well as the tools required to manufacture both silicon chips and magnetic disk drives.

In an HDD, data is stored as tiny-magnetized regions within an ultra-thin magnetic layer, the magnetic media, that is prepared on a glass disk. This layer is typically a granular ferromagnetic (FM) thin film [1–3]. The data is written into the media by small magnetic fields generated in a write head that, together with a read head, forms the magnetic recording head that is moved over the surface of the media mechanically. Today, the media is magnetized in a direction perpendicular to the surface of the disk that allows for higher density of packing of the magnetic bits. As mentioned above, the read head is formed from a spintronic magnetoresistive (MR) device, the spin-valve, that originally was all metallic, in which the MR originated from spin-dependent scattering, often described as giant magnetoresistance (GMR) [4,5] or from spin-dependent tunneling, that is referred to as tunneling magnetoresistance (TMR) [6–8]. The emergence of spin-valves based on GMR or TMR can be considered as opening the ever-expanding field of spintronics.

A spintronic device utilizes the spin degree of freedom in storing and transmitting information [9]. Such devices can display highly useful properties, such as non-volatility, low energy consumption, fast processing speed, and scalability to tiny dimensions that, thereby, allow for high density. A spintronic device usually comprises several magnetic layers and non-magnetic layers stacked together. A typical spintronic device is the magnetic tunneling junction (MTJ), as illustrated in Figure 1(a) for an in-plane MTJ (i-MTJ) where the magnetization in both FMs lie in-plane and for a perpendicular MTJ (p-MTJ) where the magnetization lies normal to the plane.

The MTJ is the main building block of the magnetic random access memory (MRAM) [10–13], an emerging non-volatile memory among others, such as resistive random-access memory (RRAM) [14], phase-change memory (PCM) [15], and ferroelectric random-access memory (FeRAM) [16]. An MTJ consists of two FM layers separated by a thin tunneling dielectric layer, usually magnesium oxide (MgO) for achieving high TMR [17–22], as shown in Figure 1(a). The resistance of the MTJ, which represents the magnetic bit, is determined by the relative magnetization orientations of the two FM layers. Typically, parallel magnetizations result in a larger probability for tunneling in the MTJ and hence a lower resistance ("0" state), and anti-parallel magnetizations result in a lower probability for tunneling and hence a higher MTJ resistance ("1" state). The magnetization of one FM layer is fixed in one direction, whereas the magnetization of the other FM layer can be altered by using current induced magnetic fields [23] or spin polarized currents generated from spin-transfer torques (STTs) [24,25] or spin-orbit torques (SOTs) [26–29].

Typically, an MRAM bit cell is composed of one MTJ and one or several access transistors. Figure 1(b) sketches the 1-transistor-1-MTJ (1T1J) configuration used in spin-transfer torque random access memory (STT-MRAM). The density of the memory not only depends on the size of the MTJ, but also on the footprint of the access transistors, which, today must be larger in area than the MTJ, to generate enough current to switch the MTJ reliably.

To reduce the cost per bit of the memory, the research community and the semiconductor industry have put considerable efforts into increasing the density of memory devices. The storage density can be increased by reducing the size of the bit by scaling down the MTJ size and by reducing the size of the access transistors by optimizing the critical switching fields or currents of the MTJ. The storage density has been increased in this way by means of material selection [30–33], device optimization [34–36], and cell architecture design [37,38]. Another path to increase the storage density is to use multi-state MTJ devices in bit cells, thus increasing the number of bits in a single bit cell. The multi-state approach is, in principle, an efficient way to boost memory density, and it is of great current interest [39–41].

In addition to enhancing the memory storage density, multi-state spintronic devices also enable brain-like, neuromorphic computing concepts [42]. Conventional computers use the von Neumann architecture [43] where the central processing unit (CPU) and main memory are separated. The mismatch between the fast CPU processing speed and slow data transfer rate between CPU and memory limits the work efficiency of conventional computers, an effect also known as the von Neumann bottleneck [44]. Significant efforts have been applied to overcome the von Neumann bottleneck, including, for example, using cache memory [45] or by the miniaturization of transistors. These technologies have led to tremendous improvements in the processing speeds of conventional computers for which the relative amount of data processed per clock cycle is relatively small. Secondly, the Joule heating associated with the transfer of data between memory and CPU leads to additional energy consumption. As a result, there is much interest in exploring novel ideas that could allow for more energy-efficient computing. This becomes ever more important as the quantities of data created by the billions, if not trillions of devices connected to the internet, explodes. Over the past 10 to 15 years, we have gradually moved into the era of "big data".

A computing system for efficiently storing and processing big data needs to possess at least two capabilities. First, it should perform both storage and processing functionalities locally, and second, it should carry out computing not only digitally, but also in analog form. These two capabilities can overcome the von Neumann bottleneck encountered in conventional computers and guarantee high computational efficiency for next generation computing. The human brain stores and processes information similarly, and, by contrast with conventional computers is orders of magnitude more energy efficient. For these reasons the research field of brain-inspired computing (neuromorphic computing) has become of ever-increasing interest as an alternative path to highly efficient computing and storage for some specialized applications.

Human brains are comprised of various types of cells wherein the main components are neurons connected with synapses (Figure 1(c)). A neuron typically consists of a cell body, an axon and multiple dendrites [46]. The axon transmits electrical and chemical signals that the dendrites receive from other neurons through many synaptic connections. The neurons may be considered in large part as processing units and the synapses as storage and learning units. The synapse assesses the importance of the information received from the pre-synaptic neuron and subsequently passes the weighted information to the post-synaptic neuron.

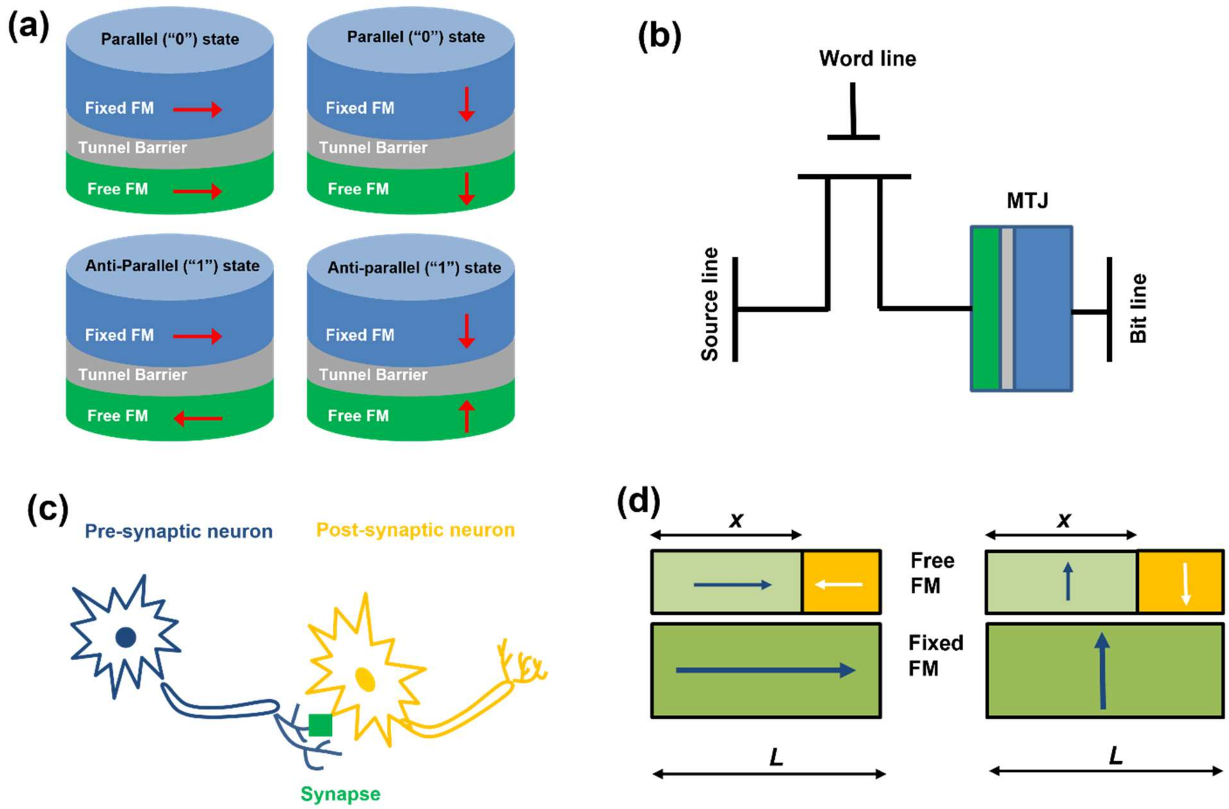

Figure 1. (a) Schematic of in-plane MTJ and perpendicular MTJ in parallel state ("0") or anti-parallel ("1") state for in-plane MTJ (i-MTJ) and perpendicular MTJ (p-MTJ). (b) Circuit diagram of an STT-MRAM bit cell in 1-transistor-1-MTJ (1T1J) configuration. (c) A synapse connecting two neurons in a biological neuron structure. (d) MTJs with domain-wall motion in the free layer for in-plane magnetizations and perpendicular magnetizations.

The ability of the human brain to store and process information locally and concurrently inspired researchers to exploit novel hardware architectures that could mimic to some extent some of the biological thinking capabilities of the human brain. This so-called neuromorphic computing dates back to the 1940s [47]. Recent advances in emerging non-volatile memories (NVM) and memristors [48–52] has accelerated the development of neuromorphic computing hardware. Various types of materials have been explored to mimic the function of a neuron or synapse in a single nanoelectronic device within RRAM [53–55], PCM [56–59], and spintronic memory technologies [60–63]. Of these technologies, spintronic devices have become one of the most encouraging candidates for neuromorphic computing. MTJ-based spintronic devices can be designed to function as either neurons [64–75], or synapses [73,76–84], and have attracted increasing attention in the research community recently [85,86]. In particular, multi-state spintronic devices are especially suitable for building synapses due to their excellent properties such as ultrafast dynamic controllability, non-volatility, low-energy, and almost unlimited endurance; traits that are also demonstrated by synapses in the human brain.

In this article, we review recent research developments and advancements in spintronic multi-state devices for high-density memory and neuromorphic computing. We focus on the materials and device structure concepts. We also discuss the prospect of using spintronic-device-based artificial neurons and synapses to accelerate both research and the eventual application of spintronic devices in neuromorphic computing for artificial intelligence (AI).

II. MULTI-STATE DEVICES BASED ON DOMAIN WALL MOTION

The resistance state of a spintronic spin-valve device is dictated by the magnetization patterns in the magnetic free layer. In a small device, e.g., the device diameter is less than 40 nm in perpendicularly magnetized MTJs [87,88], the magnetizations prefer to keep a single-magnetic domain state because of the large exchange interaction energy, which can be expressed as

$$E_{exc} = J \cdot (S_1 \cdot S_2), \tag{1}$$

where J is the exchange constant, and S_1 , S_2 are neighbouring magnetic moments. However, the magnetization of the free layer in a large device can break up into several magnetic domains that are separated by domain walls. The ability to nucleate, propagate and stabilize domain walls is crucial to achieving a multi-state spintronic device.

A. Domain wall motion in continuous magnetic nanowires

A domain wall refers to the transition region between two oppositely magnetized magnetic domains [89]. Figure 1(d) illustrates domain wall motion in a spintronic device. The MTJ has an elongated stripe shape with length L, and the domain wall position x in the magnetic free layer can be driven using a magnetic field or an electric current. The MTJ conductance $G(x)$ (inverse of resistance) is governed by [90]

$$G(x) = G_P \frac{x}{L} + G_{AP} \left(1 - \frac{x}{L}\right) + G_{DW}, \tag{2}$$

where G_P, G_{AP}, and G_{DW} are the parallel, antiparallel conductance, and the conductance in the domain wall region, respectively. All these parameters are device specific constants.

In MTJ based domain wall devices that rely on STT to dive the domain wall motion, the applied electric current is passed through the MTJ typically in a two-terminal device configuration [77,91,92]. Wang *et al.*[93] illustrated the basic theory of the memristor effect in such STT induced domain wall motion. Sbiaa and Piramanayagam [94] proposed a domain wall device with multiple resistance states for achieving multilevel storage. Lim *et al.*[91] experimentally studied the domain wall motion in an in-plane magnetization configuration driven by STT in 2004. A current pulse as short as 0.4 ns can displace the domain wall in a 300 nm wide, 30 μm long NiFe spin-valve strip with a critical current density of $10^{10}\ A/m^2$. A square pad of $1\ \mu m\ \times 1\ \mu m$ was attached at one end of the strip to assist the domain wall injection. Another method to nucleate a domain wall in planar nanowires using device temperature was investigated by micromagnetic simulations [95], where the authors discussed various device geometry effects on the domain patterns. He and Fan [92] investigated the domain wall motion in a perpendicular anisotropy nanowire driven by STT as spintronic weight devices in a reconfigurable spintronic threshold logic gate design. Two fixed magnetic domains with opposite directions are attached to the ends of the free ferromagnetic layer. They achieved a steady domain wall motion with domain velocity of up to 60 m/s in a 20 nm wide nano-strip at a critical current density as low as $6 \times 10^{11}\ A/m^2$. Lequeux *et al.* [81] experimentally demonstrated a multistate resistive switching using STT in a perpendicularly polarized magnetic strip. They fabricated samples with several track widths of 90 nm, 100 nm and 110 nm with a large nucleation pad attached at one end. Figure 2(a) depicts the side view of an MTJ device with a domain wall in the free layer, with the domain wall width denoted as Δ in the figure. Figure 2(b) is an SEM image of the MTJ from the top side. The current passing through the MTJ controls the direction and displacement of the domain wall motion. Figure 2(c) shows the MTJ resistance as a function of the current, showing multistate switching of the device. Figure 2(d) indicates that the domain wall in the magnetic wire exhibits both Neel and Bloch hybrid wall configurations. The current density required for moving the domain wall was reported to be very low, on the order of $10^{10}\ A/m^2$. However, such a current density is still too high for the needed domain wall motion in two-terminal STT devices as this current passes directly through the MTJ, resulting in reliability issues as the electric field across the tunnel barrier approached the breakdown strength. For this reason, researchers continue to explore other possible switching schemes.

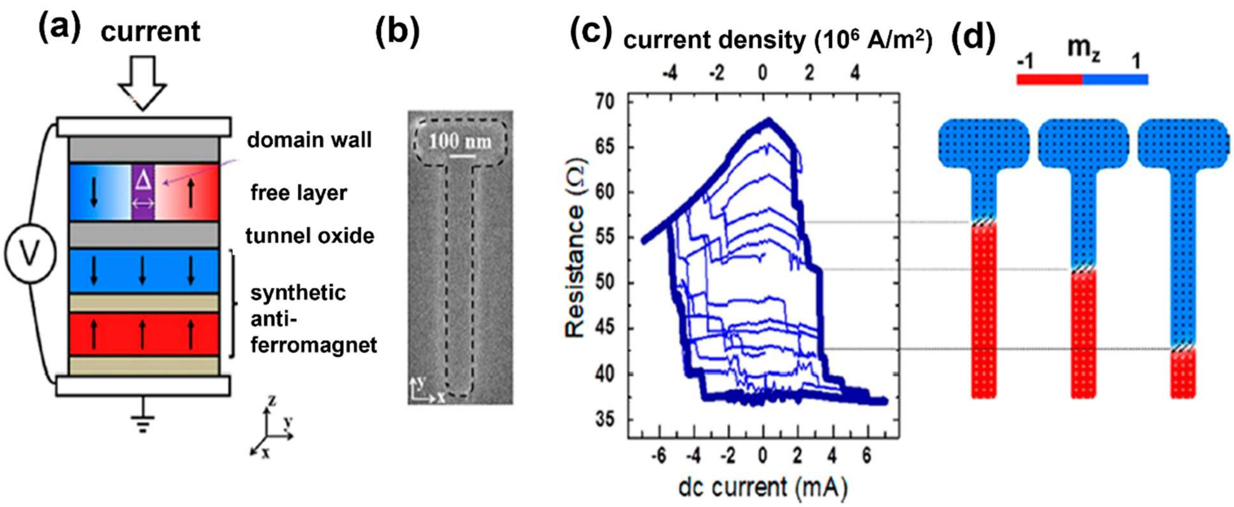

Figure 2. (a) Schematic of an MTJ with a domain wall in the free layer (side view). (b) SEM image of the MTJ (top view). (c) Resistance as a function of the injected current with an external magnetic field Hz = 85 Oe. (d) Micromagnetic simulations showing the domain wall propagation and stabilization in a 100 nm width magnetic track [81].

Domain wall motion in perpendicularly magnetized devices using SOT generated by injecting an in-plane electric current into heavy metal/ferromagnet bilayer structures has recently attracted significant attention [96–103]. In such structures, the spin-Hall effect [28,30,31] (SHE) produces the required current induced torque, and the interfacial Dzyaloshinskii–Moriya vector exchange interaction [104] (DMI) induces domain walls with a given chirality. The DM interaction between two neighboring spins has the following form,

$$E_{DMI} = -D_{12} \cdot (S_1 \times S_2), \tag{3}$$

where D_{12} is the DMI vector determined by the underlying symmetry of the crystal lattice on which the spins sit. DMI is an antisymmetric exchange promoting chiral spin textures.

The combination of SHE and DMI promotes the uniform motion of domain walls with high efficiency [97,105–108]. Figure 3(a) depicts the concept of such a three-terminal MTJ device for achieving the SOT induced domain wall motion in a free layer magnetic strip. The strip is separated from the fixed layer by inserting a tunneling oxide layer, and the domain wall position in the free layer strip determines the resistance state of the MTJ.

Passing a charge current through the Heavy Metal (HM) layer between T1 and T3 can displace the domain wall. The direction of the charge current determines whether the domain wall moves left or right. The amplitude and length of the charge current pulse dictate the distance moved, resulting in a change of the MTJ resistance that is sensed by passing a small bias current through T2 and T3.

Spintronic devices using three-terminal SOT-induced domain-wall motion have several advantages over two-terminal STT devices [109,110]. First, a two-orders of magnitude lower current density are required to produce the same amount of domain wall displacement achieved using STT. Furthermore, the spin-charge conversion for SOT devices can be more efficient than that for STT. In addition, the decoupling of reading and writing paths enables the independent design optimization for the reading and writing operations. Most of all, the write current used for driving the domain wall does not result in dielectric breakdown within the MTJ, as with STT. Figure 3(b) shows a simulated SOT-induced domain wall velocity in a perpendicularly magnetized nanowire by micromagnetic simulations [111]. The inset shows a snapshot of the magnetization pattern with a chiral domain wall. A domain wall velocity of 125 m/s was achieved with a current density of less than $2.5 \times 10^{11}\ A/m^2$.

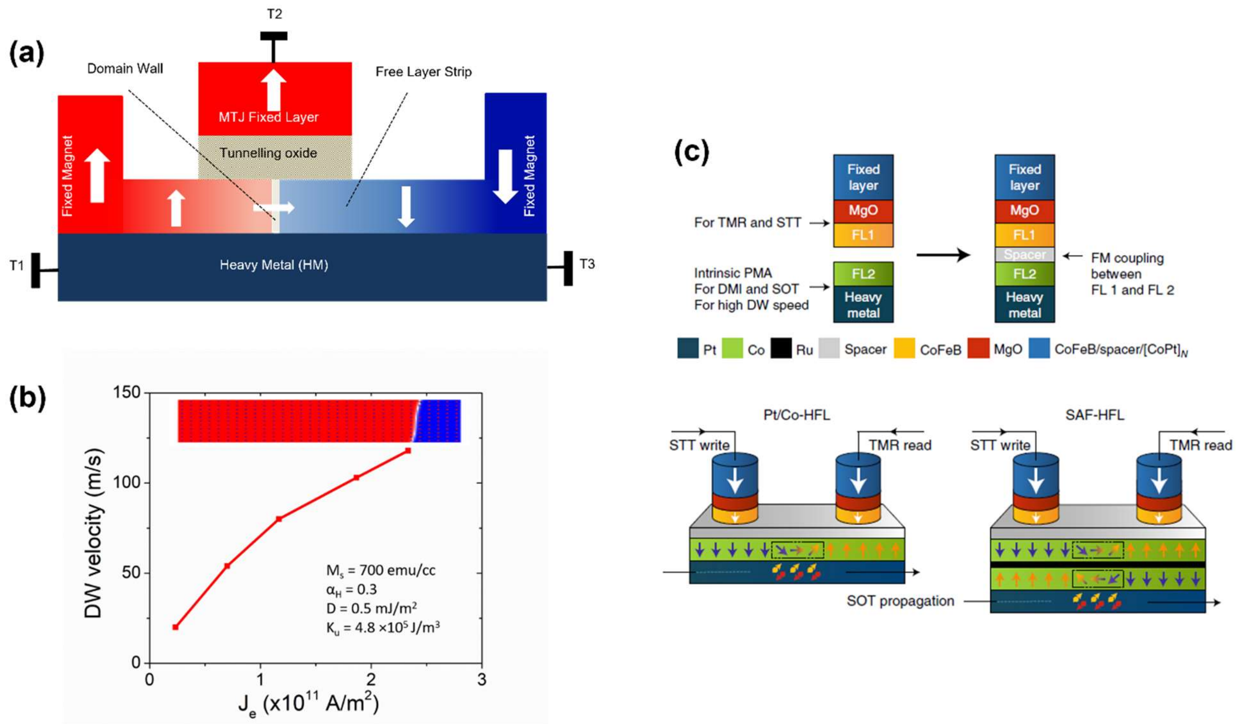

Figure 3. (a) Three-terminal domain wall motion spintronic device. During writing, a charge current passes between T1 and T3 to induce a spin-orbit torque via spin polarized electrons diffusing into the free layer strip, which displaces the domain wall. The position of the domain wall dictates the resistance state of the MTJ, which is sensed by passing a small current through T2 and T3. (b) Simulated SOT-induced domain wall velocity in a nanowire calculated by micromagnetic simulations. The inset shows a snapshot of a magnetization pattern with a chiral domain wall. Here Ms, αH, D, and Ku are saturation magnetization, spin Hall efficiency, DMI constant, and perpendicular anisotropy, respectively [111]. (c) Schematic of hybrid free layer that consists of a conventional MTJ with FL 1 for efficient STT and high TMR and FL 2 with inherent PMA optimized for high domain wall velocity driven by SOT. The two FLs are ferromagnetically coupled; schematic of domain-wall based Pt/CO devices, and schematic of SAF FL 2 design [103].

The merits of SOT-induced domain-wall-motion devices have attracted numerous research efforts aiming to develop and advance applications in neuromorphic computing architectures [82,90,102,103,112]. Sengupta et al.[90] carried out a complete device- and system-level computer simulation with a free layer strip 160 nm wide and 0.6 nm in thickness. It was shown that the velocity linearly increases with the charge current density and reaches a saturation value when the current density exceeds $2.0 \times 10^{12}\ A/m^2$. The system level simulation in the neural network for a standard pattern recognition problem indicates that the energy consumption is reduced by 100 times relative to a corresponding CMOS implementation. A method to enhance the domain wall motion velocity is demonstrated by using ion irradiation induced interface intermixing [113].

Raymenants *et al*.[103] recently proposed a SOT-induced domain-wall-motion device using a hybrid free layer (HFL) that offers a solution to device integration challenges in domain-wall based devices with a single free layer [114]. The HFL consists of a conventional MTJ attached on top of a platinum/cobalt layer or a synthetic antiferromagnet layer (Pt/Co/Ru/Co), as shown in Figure 3(c). The HFL consists of a conventional MTJ with a free layer FL 1 for efficient STT and high TMR on top of another free layer, FL 2 with inherent PMA optimized for high domain wall velocity driven by SOT. The two FLs are coupled ferromagnetically through the spacer.

During operation, an STT current is passed locally through the input pillar, injecting a domain wall into the HFL. The domain wall is moved along the HFL using SOT and its position is detected by TMR. A HFL based on a SAF offers the potential for reliable DW motion and faster write speeds compared to a device based on Pt/Co [115].

Besides STT and SOT, external magnetic fields can also induce domain wall motion in magnetic wires as shown by Kim *et al*.[116] in their experimental work for application as a neuromorphic computing device. The device consists of a single Hall-cross 10-micron in width fabricated using Co/Pt multilayers with a perpendicular anisotropy. A nucleation pad was used to create a bubble-like reversed domain at one end of the magnetic wire. A magnetic field pulse was applied along the perpendicular direction to expand the reversed domain.

B. Multi-state with synthetic pinning sites in nanowires

In smooth ferromagnetic wires, as discussed in the previous subsection, the pulse amplitude and width of the magnetic field or electric current was tuned to control the domain wall position. Hence, the pulse amplitude and width need to be precisely controlled for a given domain wall position. However, in the absence of the magnetic field or electric current, the domain wall tends to drift to the device center to minimize the total magneto-static energy [117]. For multi-state applications in magnetic memory, it is crucial to control the domain wall position precisely. This control can be achieved by using various domain wall pinning schemes [118–126], based on geometrical features or based on modification of magnetic properties. Pinning techniques such as staggered magnetic wires [127–131], notched geometries [117,132–134], and meander domain wall devices [135] belong to a geometrical approach. Modification of magnetic properties, such as modification of local magnetic anisotropy [136–139], local composition [140–142], local magnetic interactions [143] can also be used to pin the domain walls.

Figure 4(a) illustrates a representative device using staggered magnetic wires [129]. The magnetic wire is usually NiFe or CoFe for in-plane anisotropy [129] and Co/Ni multilayers are used for perpendicular magnetic anisotropy [130]. The offset parameters dictate the pinning strength and a domain wall velocity of about 200 m/s was reported for NiFe magnetic wires.

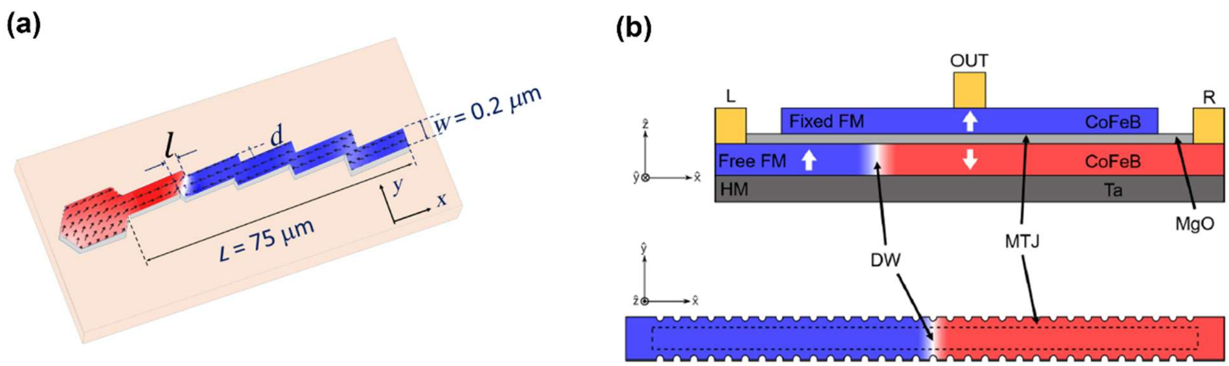

Figure 4. (a) Schematic of a staggered magnetic wire with a nucleation pad and the offset l in length direction and d in width direction [129]. (b) Side view of the domain-wall-motion device with a domain wall in the free layer, and top view of the free layer with regular pinning notches [117].

Figure 4(b) depicts the commonly used notched geometry to create pinning sites in magnetic wires for domain-wall-motion devices either with in-plane magnetic anisotropy [132] or with perpendicular anisotropy [117,133,134]. The notched devices are particularly useful as synapses in artificial intelligence neuromorphic computing hardware. The output resistance is linear and reproducible with either STT or SOT mechanisms for domain wall motion.

Other novel designs on domain-wall motion devices include a ring-shaped nanowire driven by voltage [144], and vertical-STT-current-induced domain-wall motion with a half ring structure [145]. The former design has the merit of ultra-low heat generation of 0.2 fJ, a magnitude of approximately three orders smaller than that of the conventional current-driven cases; while the latter overcomes poor intrinsic torque [146,147] efficiency acting on the domain walls from conventional in-plane-current injection.

III. MULTI-STATE DEVICES BASED ON DOMAIN NUCLEATION

Domain-wall based spintronic devices rely on the rich array of magnetization patterns to achieve multiple resistance states. Magnetization reversal in the magnetic free layer is either via coherent or incoherent modes, with the latter dominated by domain-wall motion or domain nucleation. Domain-wall motion discussed in the previous section is prone to pinning effects of various defects [148,149]. Magnetic skyrmions [150,151] may reduce pinning issues owing to their intrinsic topological nature and particle-like characteristic [152]; however, the control of magnetic skyrmions is still in its preliminary stage. Spintronic devices based on domain nucleation provides an alternative solution to achieve multiple resistance states. Figure 5(a) visualizes the difference between the magnetization pattern changes for domain-wall motion and domain nucleation devices.

Wan *et al.*[148] proposed a domain nucleation model to describe the magnetization dependence on the applied current density and the external magnetic field for SOT induced domain nucleation and propagation in the ferromagnetic free layers of a Pt/Co/MgO structure with a size of 120 µm × 30 µm:

$$\frac{dm}{d\tau} = k_0 \cdot \exp\left(-\frac{E_C}{k_B T}\right) \cdot (1-m) \cdot \pi r_C^2. \quad (4)$$

Here m is the switched magnetization, τ is SOT torque, k_0 is the attempt-frequency-related scaling factor, $\exp\left(-\frac{E_C}{k_B T}\right)$ is the thermally activated switching probability with E_C being the energy barrier needed to nucleate a domain, which is dependent on both the anisotropy K_u and external field H_x . r_C is the critical radius of the nucleated domain.

A focused ion beam was applied to a part of the Co free layer for locally reducing the anisotropy. As a result, a gradual magnetization reversal via nucleation of numerous domains with small sizes was achieved under applied current and external field. The intermediate states are detectable by sourcing the proper current.

In this section, we discuss various materials and structural designs used to obtain multistate devices based on such domain nucleation mechanisms.

A. Ferromagnet (FM)/Antiferromagnet (AFM) heterostructures

AFM materials, such as PtMn or IrMn, facilitate multi-domain formation thanks to the absence of long-range exchange interaction and magneto-static fields. In FM/AFM structures, the AF domain patterns affect the nucleation of multi-domains in FM layer under an external field or electric current, resulting in non-coherent switching of the FM magnetization. As shown in Figure 5(b) for the FM/AFM structure in a 10-µm-width Hall-bar, where FM is Co/Ni multilayer with perpendicular anisotropy, and AFM is PtMn [80], the measured relationship between the Hall resistance and the applied current indicates that the reversed magnetization amplitude can be continuously controlled by the applied current. Such a concept was used as a synapse device in the demonstration of associative memory operations [83], and in asynchronous spiking neural networks [73]. Kurenkov *et al*. [153] investigated the device size effect on the multi-state switching behaviors in such heterostructures. As the size increases from 50 nm to 5 µm, the switching changes from stepwise to several intermediate states to analogue-like behaviors. At the same time, the number of the intermediate states increases with increasing size. Fukami *et al*. [154] reviewed their studies on implementing such heterostructures as artificial neuron and synapse devices and their applications in low-energy neuromorphic computing. Multi-state switching in other FM/AFM heterostructures such as in Pt/Co/IrMn tri-layer has also been studied [155–158].

The exchange bias from the interfacial coupling between FM and AFM layers plays a crucial role in the switching of such FM/AFM heterostructures [80,155,159].

B. Modification of local material properties

Another way to introduce multi-domains into the magnetic free layer is to modify the microstructure, resulting in local material property changes for facilitating the formation of domains. The microstructure of the magnetic layer can be locally modified using ion beam irradiation such as in a 10-µm-wide Pt/Co/W Hall-bar [160] and a 5-µm-wide W/CoFeB/MgO Hall-bar [161] to locally reduce anisotropy, as well as in Ta/Pt/Co/Pt Hall device [142] to modify the local exchange constant. Researchers also used focused ion beam (FIB) irradiation technology to change the anisotropy locally in Pt/Co/MgO Hall-bar structures with a size of 120 µm x 30 µm [148]. Ion irradiation was also used to enhance domain wall velocity through interface intermixing [113].

C. In-plane field assisted domain nucleation

In SOT-induced switching of the magnetic free layer with perpendicular anisotropy, an in-plane magnetic field can tilt the magnetization within the domain wall to induce an effective perpendicular field acting on the domain wall. By varying the in-plane field, the domain patterns in the free layer are thus controllable, resulting in multi-state magnetization reversal. This has been demonstrated in the Ta/CoFeB/MgO system in a Hall-bar with a size of 400 µm × 50 µm [162,163]. Figure 5(c) shows the schematics of the device showing an SOT-induced switching mechanism in the CoFeB/Ta heterostructure, an optical image of the Hall-bar, the measured Hall resistance vs. current density curves for different values of in-plane fields. These results show that multiple resistance states are achievable by varying the in-plane field.

Similar studies have been carried out to demonstrate multi-state magnetization switching in 5-µm-width Co/Pt multilayers [164] and in Co/Pt Hall-crosses with dimensions of 50 µm × 5 µm at elevated temperatures [165].

SOT-induced switching of perpendicular ferromagnetic tri-layers of Co-Pt-Co was also studied [166]. In these tri-layers, the thickness and anisotropy of the two Co free layers are distinct, resulting in different critical switching current densities. On the other hand, for a fixed in-plane field along the charge current direction, the switching behaviors of the two Co free layers are opposite due to their contacting opposite interfaces with Pt layers. The device thus exhibits four magnetization configurations under different current pulse forms.

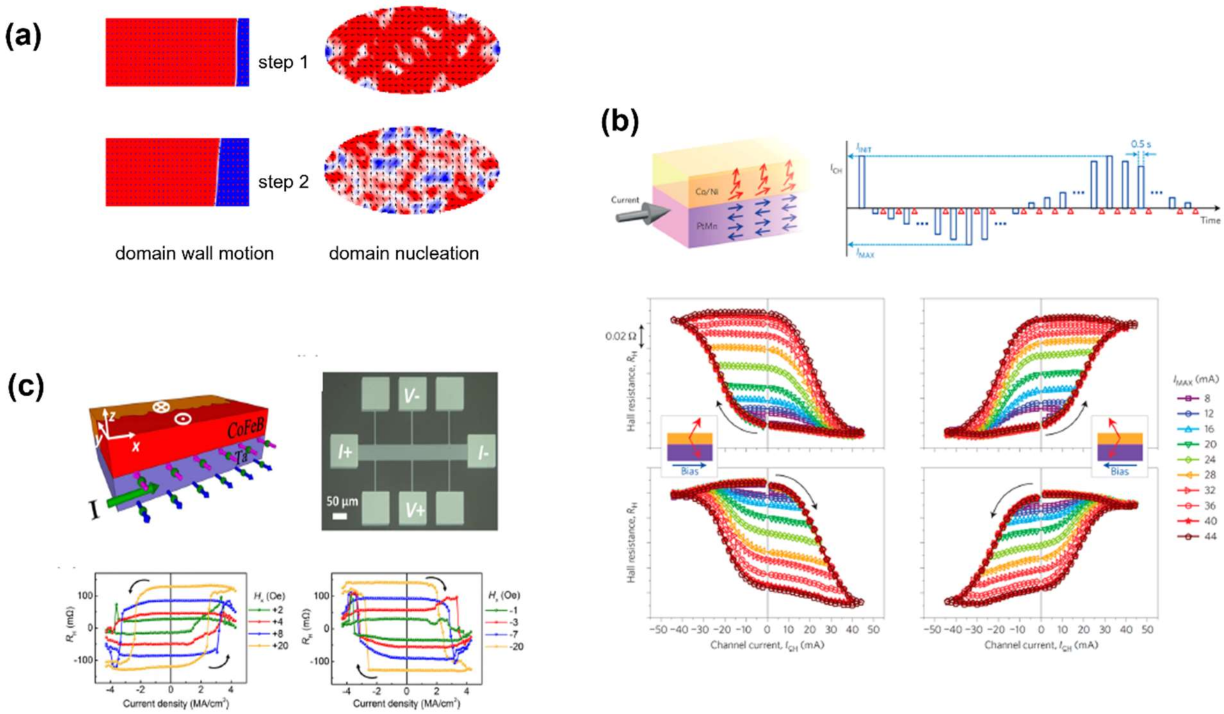

Figure 5. (a) Magnetization patterns in different steps for domain-wall motion and domain nucleation in a 500 nm × 1000 um device. (b) Schematic of FM (Co/Ni)/AFM (PtMn) structure, including recipe of measurement procedures, Hall resistance vs current loops with positive bias, and Hall resistance vs current loops with negative bias. Black-curved arrows represent the starting measurement positions [80]. (c) Schematic of SOT-induced switching in a CoFeB/Ta heterostructure, the optical image of 400 µm × 50 µm Hall-bar, and resistance vs. current density loops for different values of in-plane fields [162].

D. Field-free multi-state switching of PMA magnets

It is worth mentioning that SOT-induced field-free multi-state switching of perpendicular magnets in Ta/MgO/CoFeB/MgO heterostructures has been demonstrated using a wedged MgO layer between Ta and CoFeB layers [167]. Hall-bar devices with a width of 20 µm were patterned using standard photolithographic techniques. Figure 6(a) shows a schematic of a Ta/MgO (wedged)/CoFeB/MgO stack, a patterned Hall-bar image and measurement setup, measured results for the anomalous Hall resistance as a function of magnetic field at various wedged MgO thicknesses, and measured results for the pulse-current induced field-free switching for various

MgO thicknesses, showing a four-state magnetization switching for a wedged MgO thickness of 0.25 nm.

An alternative scheme for achieving field-free multi-state switching of PMA magnets is to use composite free layers such as in Pt/FM1/Ta/FM2 heterostructures. Here FM1 is ferromagnetic layer with PMA, and FM2 is a ferromagnetic layer with in-plane magnetic anisotropy (IMA), which is anti-ferromagnetically coupled with FM1 through a spacer layer Ta [168]. Figure 6(b) is a schematic of the PT/FM1/Ta/FM2 composite magnetic layered system and the measurement setup, the measured resistance vs magnetic field loops for various in-plane fields, and the measured resistance vs current density loop without in-plane field, showing multi-state switching. The size of the Hall-bar is 6 μm × 6 μm. Similar concepts have been adopted in other related research [169].

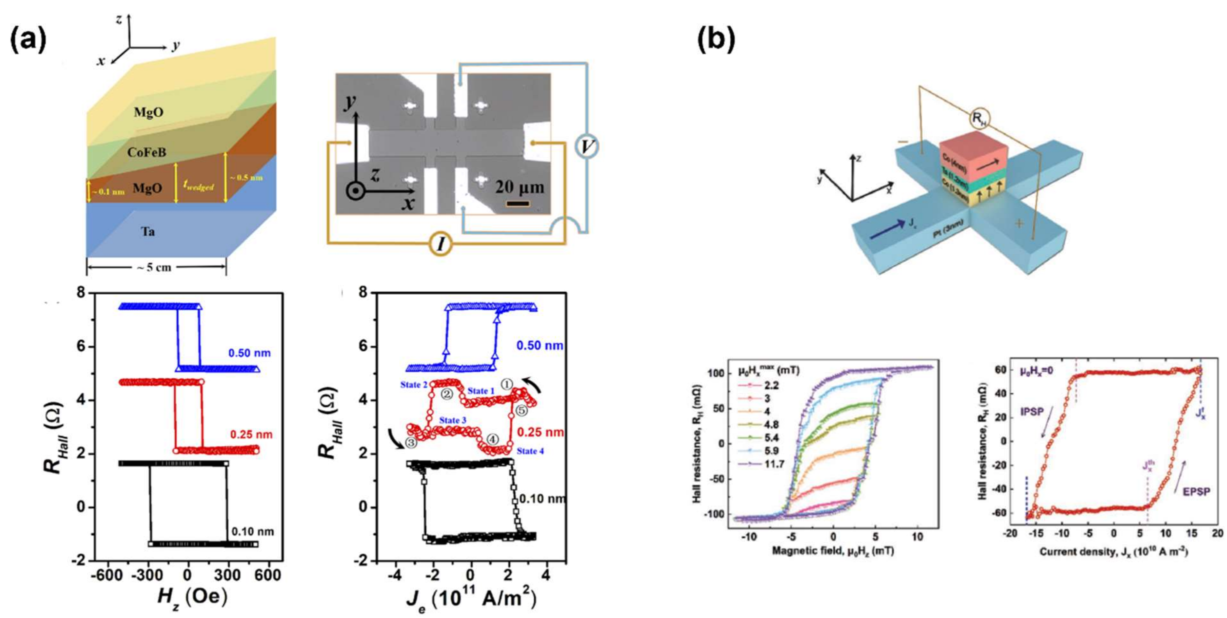

Figure 6. (a) Schematic of a Ta/MgO (wedged)/CoFeB/MgO stack, patterned Hall-bar image and measurement setup, Anomalous Hall resistance vs magnetic field for various wedged MgO thickness, and pulse current induced field-free switching for various MgO thicknesses, showing a four-state magnetization switching for a wedged MgO thickness of 0.25 nm [167]. (b) Schematic of a PT/FM1/Ta/FM2 composite magnetic layered system and the measurement setup, resistance vs magnetic field loops for various in-plane fields, and resistance vs current density loop without in-plane field showing multi-state switching [168].

E. Magnetic skyrmions and other domain nucleation devices

The characteristics of magnetic skyrmions that are controllable by electric current, including their creation, detection, motion, and deletion in a single device, offer the possibility of using them to emulate artificial synapses and neurons for neuromorphic computing and have attracted much attention [108,170–174]. Li et al. [174] reported sub-100 nm sized room-temperature skyrmions in an MTJ device, which leverages the TMR effect to directly detect the skyrmions observed by MFM techniques. The controllable nucleation of skyrmions in the MTJ under electric pulse excitation was achieved as shown in Figure 7, leading to a non-volatile multilevel analog resistance. This skyrmionic MTJ device could potentially build a complete synapse-neuron system with advantages of easily tunable resistance and resistance reproducibility by achievable control of the skyrmionic density and size. Recent reviews on magnetic skyrmions can be found both with for device concepts and memory and logic applications [175–178].

As for other domain nucleation devices, Zhou *et al*.[149] recently demonstrated current-induced magnetization switching in a single-crystalline $L1_1$-CuPt/CoPt bilayer Hall-bar structure. Multiple intermediate magnetization states were shown in the device due to the gradual domain nucleation under SOT current. Field-free multi-state switching is achievable when the charge current is passing along the low-symmetry axis.

Another interesting way to achieve multi-state devices through domain nucleation is utilizing a remanent magnetism engineering approach [179]. Ten magnetization states are achievable in both perpendicular Co/Pt magnetic multilayers and MgO-based MTJs with CoFeB free layer at room temperature using magnetic field sweeping.

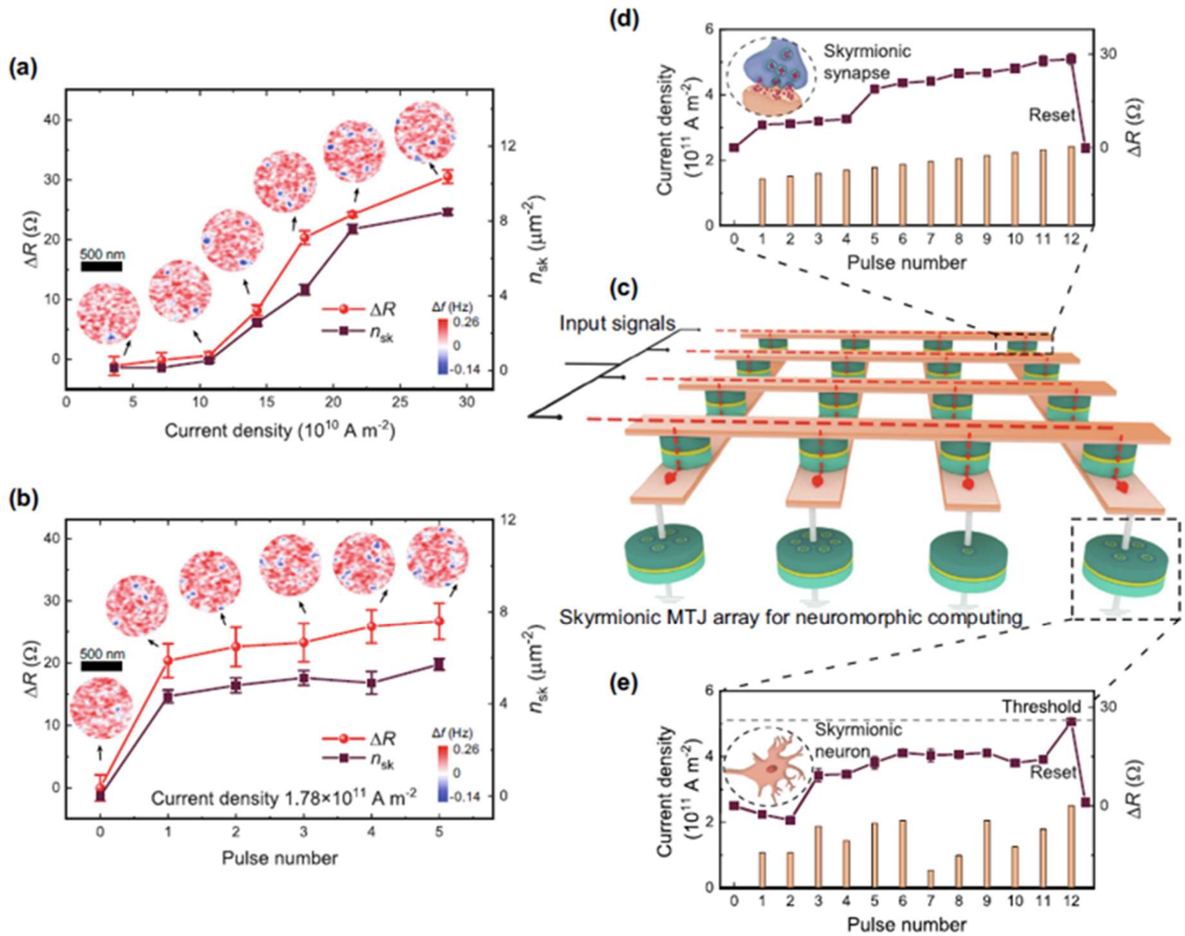

Figure 7. As a function of current density with a single pulse (a) and current pulse number (b), the variation of resistance and the induced-skyrmion density. (c) The skyrmioinc MTJ array for the neuromorphic computing. (d) Mimic of the long-term potentiation of the synapse. (e) Activation process of the neuron [174].

IV. MULTI-LEVEL CELLS IN MTJs

As mentioned above, MRAM is one of the encouraging candidates as a universal memory due to its non-volatility, high speed, infinite endurance, low energy consumption, and compatibility with complementary metal oxide semiconductor (CMOS) [11]. Two-terminal STT-MRAM has a compact cell design with shared read and write path; however, the high write current passing through MTJ results in MTJ barrier breakdown when the cell size is scaled down to increase memory density [180,181]. This limitation is circumvented with an alternative writing scheme in the three-terminal SOT-MRAM, where the write and read paths are decoupled [28,30,182]. Although SOT-induced switching addresses the reliability issues encountered in STT, it creates its own limitations on decreasing memory density, as each bit-cell in SOT-MRAM requires two transistors [37]. Design of multi-level cell (MLC) is one of the most powerful solutions to increase the memory density. Various studies using such concept include MLC in STT-MTJ [82,183–193], MLC in SOT-MTJ [37], MLC in STT-assisted with SOT MTJ [194], and MLC with domain-wall shift (DWS) MTJ [195–199]. Figure 8 illustrates the design concept and the architecture of the MLC-MTJ [37,38]. The detailed methods of write and read operations of the MLC-MTJ are shown in a review paper written in 2016 by Fong *et al.*[38]. Prajapati *et al.*[183] presented a physics-based circuit model in terms of the LLGS formalism for the MLC-MTJ. Their SPICE simulations reveal high performance of MLC-MTJ with a distinct presentation of multiple resistance states, making the device suitable for high density embedded memory applications.

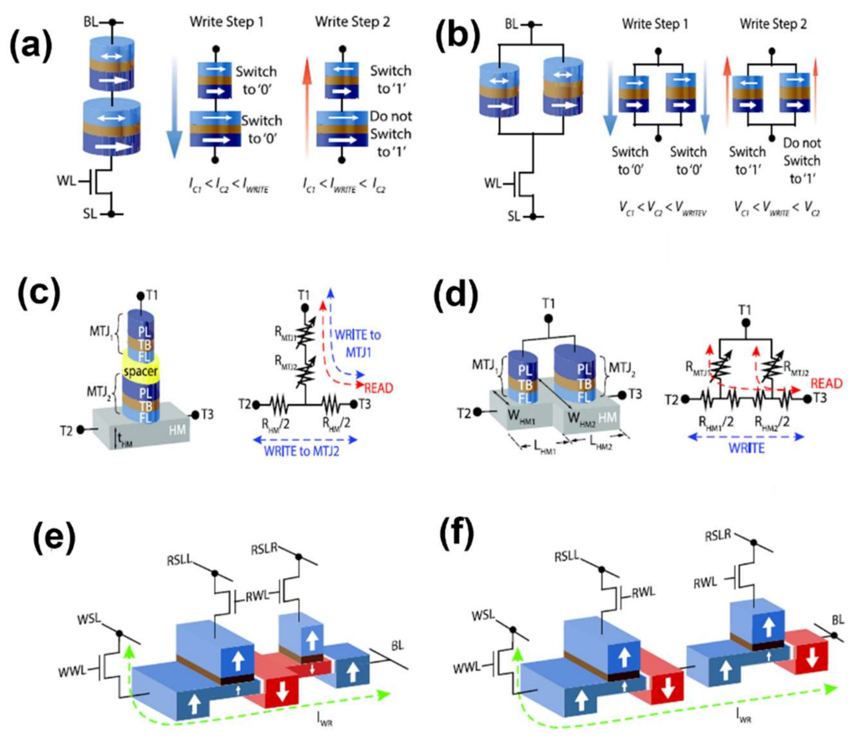

Figure 8. (a) Series-connection MLC-STT-MTJ. (b) Parallel- connection MLC-STT-MTJ. (c) Series-connection MLC-SOT-MTJ. (d) Parallel-connection MLC-SOT-MTJ. (e) Schematic of domain-wall shift memory. (f) Possible implementations of MLC-DWS-MTJ [38].

More recently, double-pinned perpendicular MTJ spin-valve was proposed and experimentally demonstrated to achieve a four-level resistance state. High tunneling magnetoresistance (TMR) ratios of 152.6%, 33.6% and 166.5%, respectively, are achievable using CoFeB as free layers [200,201]. A uniform resistance difference between the four-level resistance states exempts the device from writing and reading disturbances in the integrated memory-cells.

Hong *et al.*[202] proposed a three-dimensional (3D) configuration for vertical stacking device MTJ (3D-MTJ) with sub-20-nm size to achieve three-level switching. Figure 9(a) shows the schematic of 3D devices and two-resistance model, as well as the three resistance states and their corresponding magnetizations in the three free layers.

Hong *et al.*[203] also proposed another 3D-MTJ with a dual domain structure, as shown in Figure 9(b). Five resistance states are achievable within a single MTJ with corresponding magnetization patterns. By connecting two such two dual-domain MTJ in series, eight distinct levels of resistance states are achievable. In principle, by adding more dual-MTJs vertically, one can achieve even more resistance states in such 3D configurations. The materials of the free layer can be Co/Pt or Co/Pd multilayers whose magnetic properties are controllable through the interface as well as the thickness of the stack layers [204].

V. OTHER SCHEMES LEADING TO MULTI-STATE DEVICES

Besides achieving multiple resistance states using either domain-wall motion, domain nucleation, or 3D multilevel cell architectures as discussed previously, there are other proposed schemes for achieving multiple states. These schemes include fabricating ferromagnetic free layers with multiple easy axes [205–210], using antiferromagnetic free layers [211–213], utilizing the unidirectional spin-Hall magnetoresistance (USMR) [214], or assisting with other mechanisms such as electric field manipulated switching in PMN-PT heterostructure [215], and resistive-enhanced MTJ [216].

STT or SOT can switch a ferromagnetic free layer with a uniaxial anisotropy between the two opposite uniform magnetization states. In general, four magnetization states are achievable for a ferromagnetic free layer with biaxial anisotropy [186,206]. Figure 9(c) shows an artificial free layer shape with three crossing ellipses possessing of tri-axial anisotropy; hence, six magnetization states are achievable [205]. Ways to achieve even more magnetization states with such design of free layers were described in details in a very recent work [217].

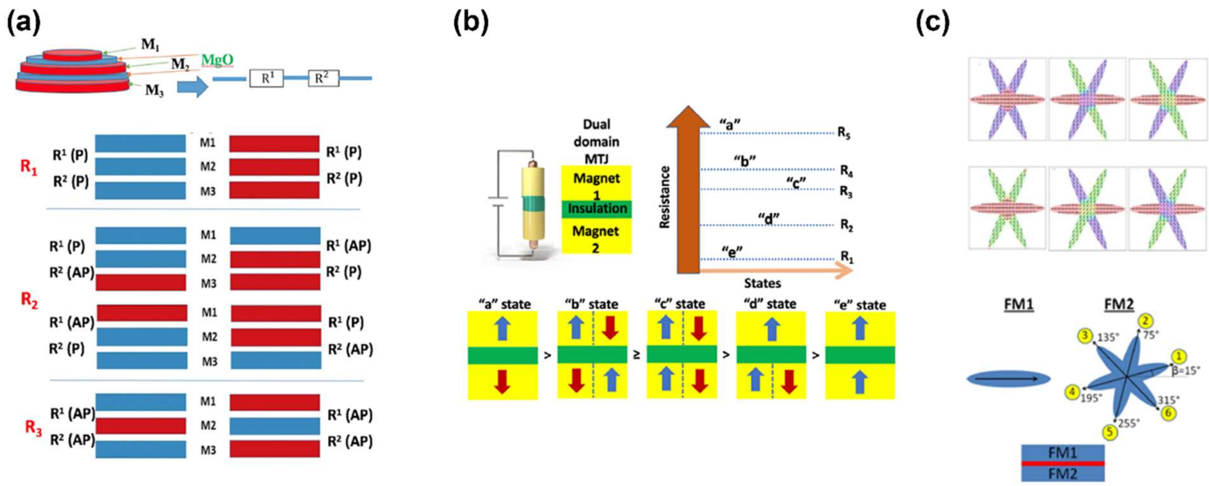

Figure 9. (a) Schematic of 3D devices and two-resistance model and three resistance states and their corresponding magnetization states in the three free layers [202]. (b) Schematic of a dual domain MTJ, the achievable five resistance states, and magnetization patterns corresponding to five resistance states [203]. (c) Simulated 6 magnetization patterns in the overlapping region of three intersecting elliptical films, and schematic of six resistive states corresponding to six different angles. FM1 is the fixed free layer; FM2 is the free layer with multiple easy-axis [205].

VI. MULTI-STATE SWITCHING IN SINGLE NANOSCALE DEVICES

As both magnetic anisotropy and Heisenberg exchange in ferromagnetic free layers promote a collinear spin texture, the stabilization of intermediate magnetization states in nanoscale devices is a challenging task under thermal activation and operation currents [218,219]. Possible solutions discussed in Sections II and III to create and stabilize intermediate states require a relatively large device at least microns in size, or need an external magnetic field to achieve.

A nanoscale device with submicron dimensions without the need for any external magnetic field is imperative in practical applications for high storage density and neuromorphic computing. The interfacial DMI, favoring a chiral spin texture, makes it possible to stabilize intermediate magnetization states in nanoscale spintronic devices, and thus it attracts numerous studies

[82,97,107,134,220–228]. Significant attention has also been paid to multi-state switching of p-MTJs with nanoscale dimensions recently.

Zhang *et al*.[229] demonstrated a spin-torque memristor spintronic device based on a PMA-MTJ with a composite free layer (CFL) incorporating the tri-layer structure CoFeB/W/CoFeB. The CFL was patterned into nano-pillars 400-nm in diameter. An electric current passing through the MTJ induces STT switching of the CFL. Figure 10(a) shows the schematic of the device stack structure and the measured results for STT switching of the device showing stable intermediate resistances. Energy fluctuation caused by the chiral spin texture may be the main reason resulting in strong domain-wall pinning effects in the device.

Multi-state STT switching for a nanoscale single free layer was also investigated for a p-MTJ based on CoFeB/MgO/CoFeB structures [230]. Three or four stable resistance states are achievable in a circular device with diameters ranging from 300 nm to 800 nm. Figure 10(b) shows the procedures used for the multi-level switching characterization, and the 3-level and 4-level switching with 400 and 800 nm p-MTJ, respectively. The insets illustrate the possible magnetization configurations of the free layer and fixed layer of the p-MTJ. In general, the free layer splits from a single domain into multiple domains with increasing device size. To obtain multi-domains in a small device, the magnetic properties need to be properly tuned.

Three-terminal SOT switching has advantages over two-terminal STT switching in terms of high speed, high endurance, and low read disturbance [182,231–233]. Lourembam et al. [234] investigated multi-state three-terminal SOT switching for i-MTJ with submicron sized single free layers. They demonstrated metastable multi-domain states in Pt/CoFeB/MgO based MTJ devices with elliptical shape of 300 nm × 1000 nm. Four resistance states are achievable in most of our devices without using any pining steps. Micromagnetic simulations reveal that the multiple resistance states in these devices originate from the metastable multi-domain states where the total energy is a local minimum in the energy landscape. Hence, multiple resistance states may not appear in small devices with sizes below the corresponding domain wall width, as such small devices tend to exhibit mono-domain behaviours.

A recent interesting simulation work [235] aims to realize multi-state switching in mono-domain MTJ devices using composite free layers in a stack of HM (heavy metal)/p-FL1(perpendicular free layer 1/CL(coupling layer)/i-FL2(in-plane free layer 2)/BL(barrier layer)/RL(reference layer) structure. When applying a charge current (with current density J_{SOT})

through the HM below the MTJ, due to the spin-Hall effect, the induced spin current controls the dynamics of the magnetization in p-FL1. It is noted that the long axis of the free layer is perpendicular to the flow of the charge current direction. As shown in Figure 10(c), thanks to the coupling effect from CL, the magnetization in i-FL2 is set to various directions at different current densities, resulting in multistate MTJ resistances. However, the intermediate states in such device as shown in B, C, E and F tends to relax to either state A or D upon the removal of the current, thus limiting the device's practical use.

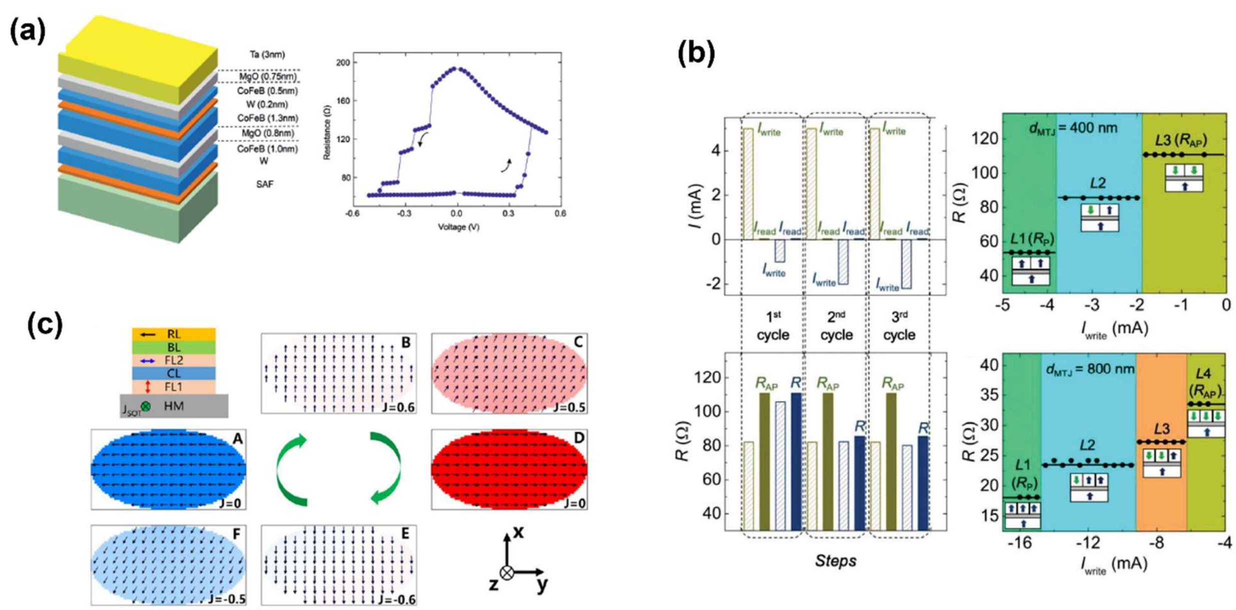

Figure 10. (a) Schematic of device stack structure, and STT switching of the device showing stable intermediate resistances [229]. (b) Multi-level switching of a p-MTJ: the measurement method indicating the applied current and the measured resistance, and the 3-level and 4-level states obtained for a diameter of 400 and 800 nm, respectively. The insets illustrate possible magnetization configurations [230]. (c) Schematic of the proposed MTJ stacks, and snapshots of magnetization patterns in the in-plane free layer (FL2) at different current densities in the unit of 10^{12} A/m^2 [235].

The works discussed above on multi-state switching in single nanoscale devices are achieved either using STT induced switching for p-MTJ or SOT induced switching for i-MTJ. To the best of our knowledge, studies on multi-state switching for nanoscale p-MTJ devices with three-terminal SOT mechanism is still lacking.

To understand the SOT induced magnetization dynamics in nanoscale p-MTJs, and to seek possible multi-state switching devices, we carry out micromagnetic studies on a p-MTJ with a circular free layer as depicted in Figure 11(a). The free layer of a diameter 1000 nm is discretised into cell sizes of 2 nm × 2 nm × 1 nm, where the free layer thickness is assumed to be 1 nm. Table 1 lists the material parameters [30,236,237] used in the simulation. Figure 11(b) depicts the average z- component magnetization m_z as a function of the current density J_e at different in-plane fields H_x. We start from single domain down magnetization ($m_z = -1$) and apply currents with gradually increasing amplitudes. Each point in the curves represents a sequence of 5 ns current pulse passing on the SOT channel followed by relaxation. The corresponding snapshots of magnetization patterns of the mid-states achieved at each relaxed point are also shown (The blue corresponds to down magnetization, and red corresponds to up magnetization). Without the external magnetic field (black curve), the magnetization is unable to switch even with sufficiently high current densities. Stable intermediate magnetization states are achievable by controlling different pulse amplitudes under external magnetic fields. Different external fields result in different intermediate magnetization states (H_x= 5, 10, 15, 20 mT). However, the intermediate states disappear at high external fields where completely reversal of the magnetization occurs (H_x= 25, 30 mT).

Table 1: Simulation parameters

Symbol	Parameter	Default value	Reference
M_s	Saturation magnetization	1.1×10^6 A/m	[30,236,237]
K_u	Intrinsic anisotropy	0.8×10^6 J/m^3	
Α	Damping constant	0.1	
A	Exchange constant	20×10^{-12} J/m	
α_H	Spin-Hall angle	0.1	
D	DMI constant	0.5 mJ/m^2	

To eliminate the external magnetic field, we add a coupling layer and an in-plane magnetic layer on top of the perpendicular layer and make the shape elliptic with the long axis along the flow of the charge current direction, as shown in Figure 11(c). Table 2 lists the simulation parameters for the composite free layer.

Table 2: Simulation parameters for the composite free layer

Symbol	Parameter	Default value	Reference
M_{sFL}	Saturation magnetization for FL	1.1×10^6 A/m	[30,236,237]
K_{uFL}	Intrinsic anisotropy for FL	0.8×10^6 J/m^3	
M_{sCL}	Saturation magnetization for CL	0.8×10^6 A/m	
K_{uCL}	In-plane anisotropy for CL	2×10^4 J/m^3	
A	Damping constant	0.1	
A	Exchange constant	20×10^{-12} J/m	
α_H	Spin-Hall angle	0.3	
D	DMI constant	0.5 mJ/m^2	

We again start from single domain down magnetization ($m_z = -1$) and apply currents with gradually increasing amplitudes. Each point in the curves represents the application of a sequence of 5 ns current pulses on the SOT channel followed by relaxation or no relaxation. Figure 11(d) shows the simulation results, indicating that field-free SOT induced multi-state switching in p-MTJ is achievable using the proposed composite free layer. The corresponding snapshots of magnetization patterns for the mid-states are also shown (The blue corresponds to down magnetization, and the red corresponds to up magnetization).

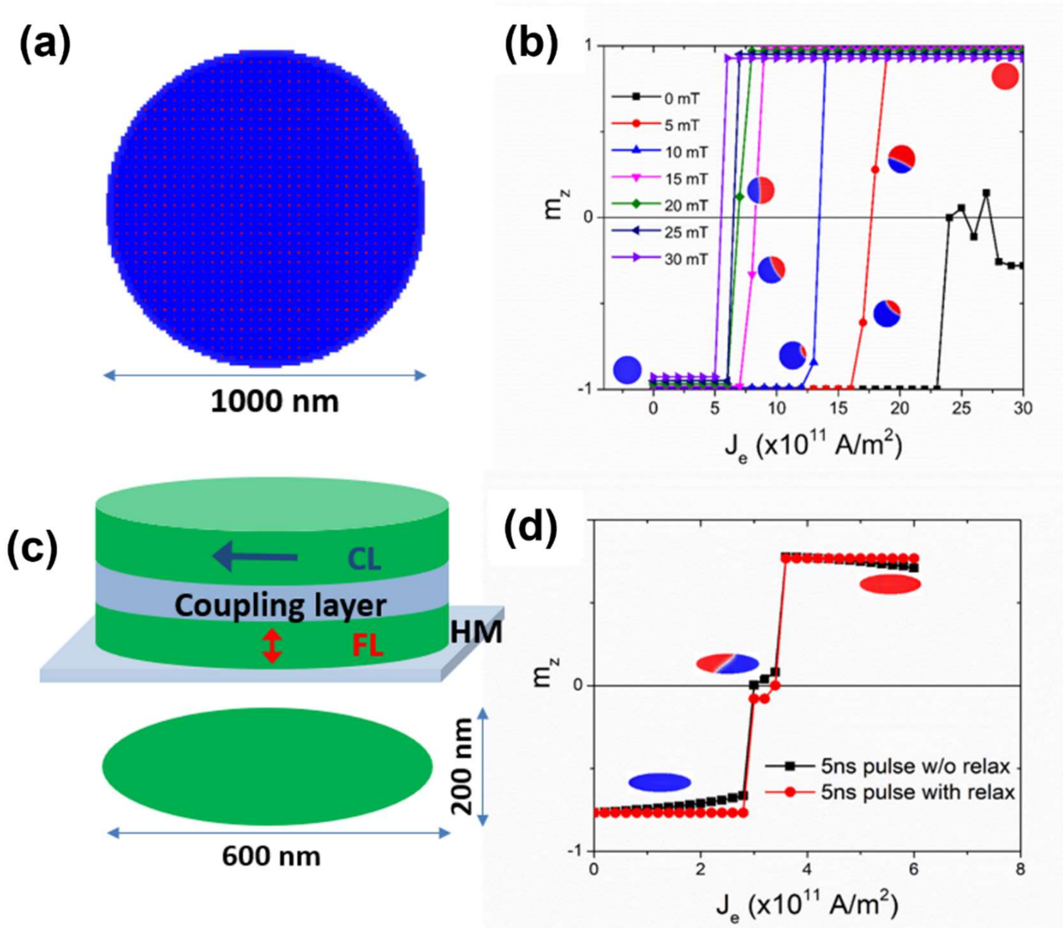

Figure 11. (a) Schematic of a single free layer 1000 nm in diameter. (b) z- component magnetization vs current density at different in-plane field, showing multi-state switching. (c) Schematic of a perpendicular free layer (FL) coupled with an in-plane free layer (CL). (d) z- component magnetization vs current density, showing field-free multi-state switching.

VII. PROSPECTS OF USING SPINTRONIC DEVICES IN NEUROMORPHIC COMPUTING

Modern AI chips using deep learning algorithms work radically differently from our brain. They solve complicated numerical problems with high precision and digital encoding, while our brain uses parallel processing with low precision and analog encoding. The brain has two key components: synapses for storing connection weights and neurons with nonlinear activation for processing information. To simulate the behavior of synapses and neurons, the use of compact and low power spintronic devices has emerged to be an area of great potential [85,86,238–240].

A. Neuromorphic computing based on Spin Torque Oscillators

Biological neurons in our brain typically work in a leaky-integrate-fire (LIF) model. Neurons continuously receive spiking trains from other neurons that increase their membrane potential to a threshold, and this triggers firing spikes. After firing, neurons undergo a refractory period and the membrane potential goes back to the resting state. The nonlinear magnetization dynamics in some spintronic devices can be tailored to mimic the LIF model. One appealing example is spin-torque nano-oscillators with nonlinear frequency and amplitude response to an external bias. Moreover, the slow decay in the oscillation amplitude can imitate the leaky integration of neurons. Furthermore, controlling the coupling and communication of spin-torque oscillators in an array offers great design flexibility and tenability for simulating the collective behaviors of neurons in the brain. In 2017, Torrejon et al. [72] demonstrated that using a spin-torque oscillator in spoken-digit recognition can attain an accuracy similar to that of a state-of-the-art neural network, as shown in Figure 12.

The spin-torque oscillator consists of two ferromagnetic layers separated by a non-magnetic spacer. A current injected into the oscillator can induce magnetization precessions and output an oscillating voltage, which is robust to noise. Moreover, the output voltage, as a function of the injected current, is highly nonlinear and depends intrinsically on the past inputs. The combined function of nonlinearity and memory enables the MTJ oscillator to work as neurons. Here, the neural input is the time-dependent current injected into the oscillator, and the neural output is the amplitude response of the oscillator. Their pattern-recognition results indicate that a simple and ultra-compact network comprising spin-torque oscillators can well mimic the neural connections. The interaction and communication between spin-torque oscillators are realized through current and magnetic field coupling. This work has greatly inspired researchers to exploit spin-torque oscillators for neuromorphic computing [241–245].

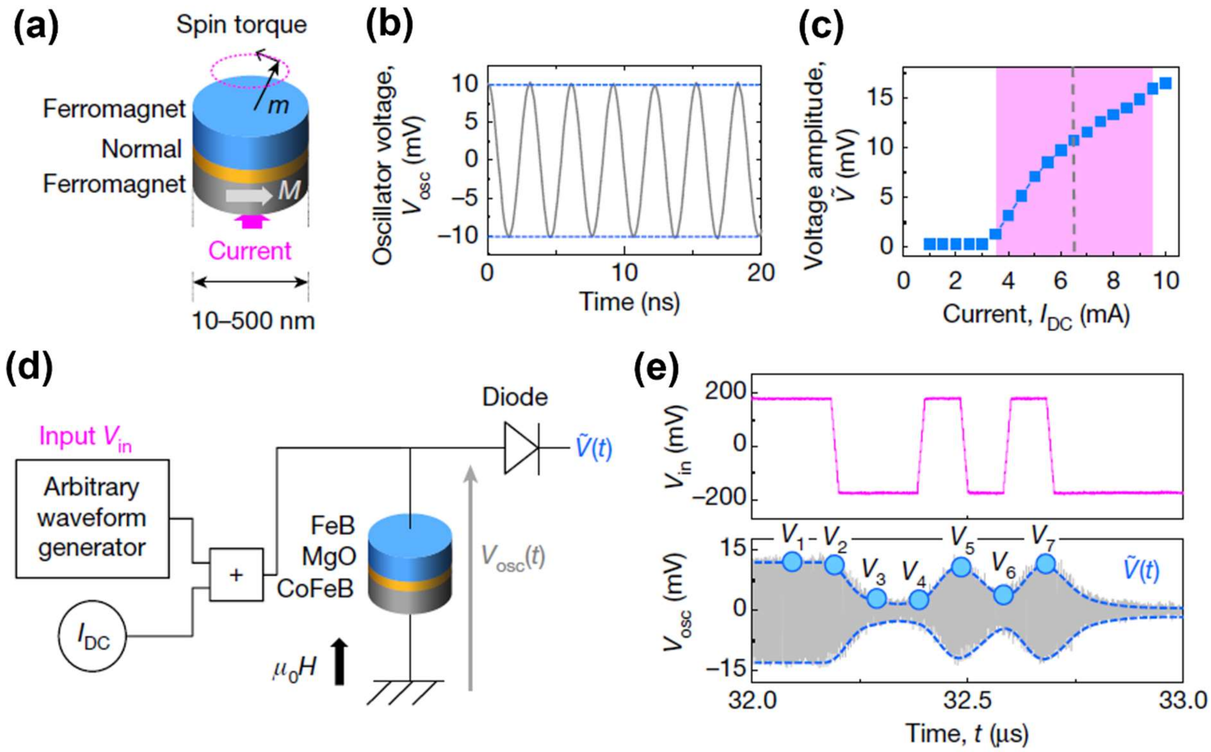

Figure 12. (a) Schematic of a spin-torque oscillator. The magnetization precession at the free layer is driven by an injected current. (b) Oscillating output voltage of the spin-torque oscillator. (c) Voltage amplitude as a function of DC current. (d) Experimental set-up. The input Vin is generated by a d.c. current and a rapidly varying waveform. (e) Time-dependent input voltage Vin and output voltage Vosc emitted by the oscillator [72].

B. Neuromorphic computing based on Skyrmions

The position and motion of magnetic textures in domain walls and skyrmions have been explored to function as neurons with their nonlinear dynamics. Using micromagnetic simulations, Li *et al*.[151] and Chen *et al*.[246] proposed skyrmion neurons exploiting the current-driven magnetic dynamic of skyrmions in a wedge-shaped nanotrack. Combining the exciting current pulse and the repulsive force (backward PMA-gradient force in [151] and wedge repulsive force by nanotrack edge in [246]) exerted by the nano-track device, the tunable current-driven skyrmion motion mimics the accumulation of membrane potential at the axon of biological neurons. Moreover, its input-output relationship of spiking trains follows the LIF model of biological neurons, as depicted in Figure 13. In the recent experiment [247], Yang et al. demonstrated a stochastic skyrmion neuron of a HM/FM/AFM heterostructure by using the competition between the SOT and AFM pinning effects. Except for LIF model, an application of a fixed skyrmion with Giga-Hertz oscillation for resonate-and-fire type neuron was proposed in [248], using the continual breathing of a skyrmion core in the MTJ device.

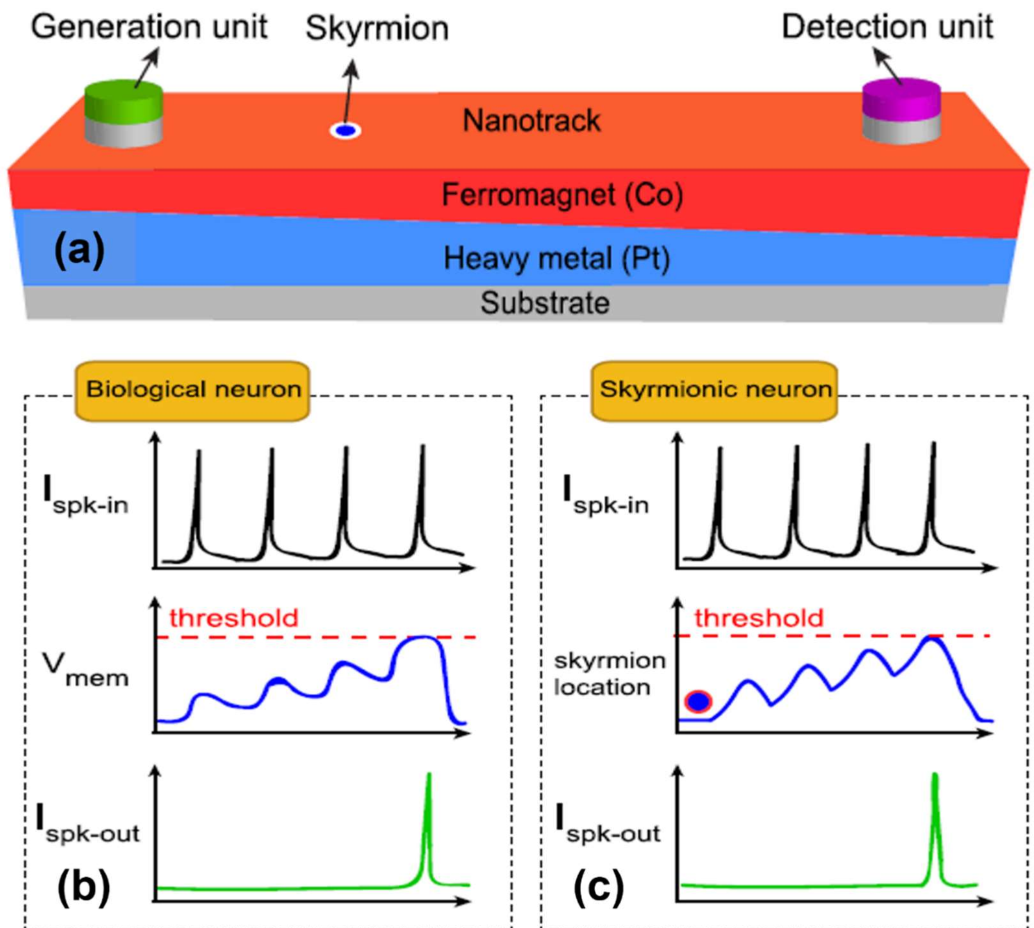

Figure 13. (a) Schematic of the skyrmion-based artificial neuron device; (b) demonstration of the LIF behaviors of a biological neuron and (c) demonstration of the LIF behaviors of a skyrmion-based artificial neuron [151].

Synapses are storage and learning units of our brain, working locally and analogically with the processing neuron units. The cooperation between synapses and neurons completes the nonlinear operation of weighted sum over received information, which is key for neuromorphic computing. Spintronic devices are well known for their storage function due to their non-volatility, ultrafast magnetization dynamics, and unlimited endurance. Moreover, the tunability of multi-state behavior in spintronic devices enable them to operate as learning units. The resistance in these devices depends on the historical activity of inputs, a property called plasticity in memristors. A linearly dependent plasticity has been found in notched geometry of domain-wall-motion devices, where pinning sites in magnetic wires account for the tunable and non-volatile resistance [117]. Besides, multi-state switching and memristive behavior have been demonstrated in FM/AFM heterostructures, where the antiferromagnetic order in the AFM layer is effectively manipulated by SOT [249]. Tuning the exchange biases in ferromagnetic domains is another effective way to realize the memristive function, where the magnetization switching loop is electrically controllable [250]. In addition, there have been reports of electrical control of creation, deletion and motion of magnetic skyrmions that can also be used to emulate synapses [251]. In Song's experiment, the synaptic weights are proportional to the number of skyrmions in a synapse. They apply electric currents to control the accumulation and dissipation of skyrmions. As a result, the variation of synaptic weights in skyrmions imitates synaptic potentiation and depression of our brain. Moreover, such a multilevel resistance state of the skyrmion device has been explored in circuit models to implement different kinds of neural networks [252,253] (e.g., ternary neural network and spiking neuron network). In addition to memristors, another important synapse model in neuroscience is spike-timing-dependent plasticity (STDP). The conductance change in the STDP model is a function of firing time-difference between post-spiking and pre-spiking trains. Spin-torque MTJs have been reported as random spiking generators and stochastic binary synapses obeying the rule of STDP [98]. Based on the temporal correlation between the spiking activities of the interconnecting neurons, the synaptic plasticity in the MTJ-HM heterostructure is attained by the stochastic switching of the MTJ conductance states.

To date, the stochastic dynamics of skyrmionic device has also been utilized to realize reservoir computing as neuron nodes in the reservoir layer [150] and stochastic computing as a true random number generator [254] and signal reshuffle device [255]. In summary, the intrinsic dynamic behaviors and particle-like nature of the skyrmion highlight its potential for neuromorphic computing in the future [256].

C. Domain wall Magnetic Tunnel Junctions based neuromorphic computing

In an earlier section, we have discussed the utilization of domain wall devices with multiple resistive states for memory applications. The same concept could also be used for synaptic applications. With a slight modification, a magnetic tunnel junction in the form of a domain wall device also could be used as a neuron. In this section, we will discuss the use of domain wall MTJs for neuromorphic computing applications.

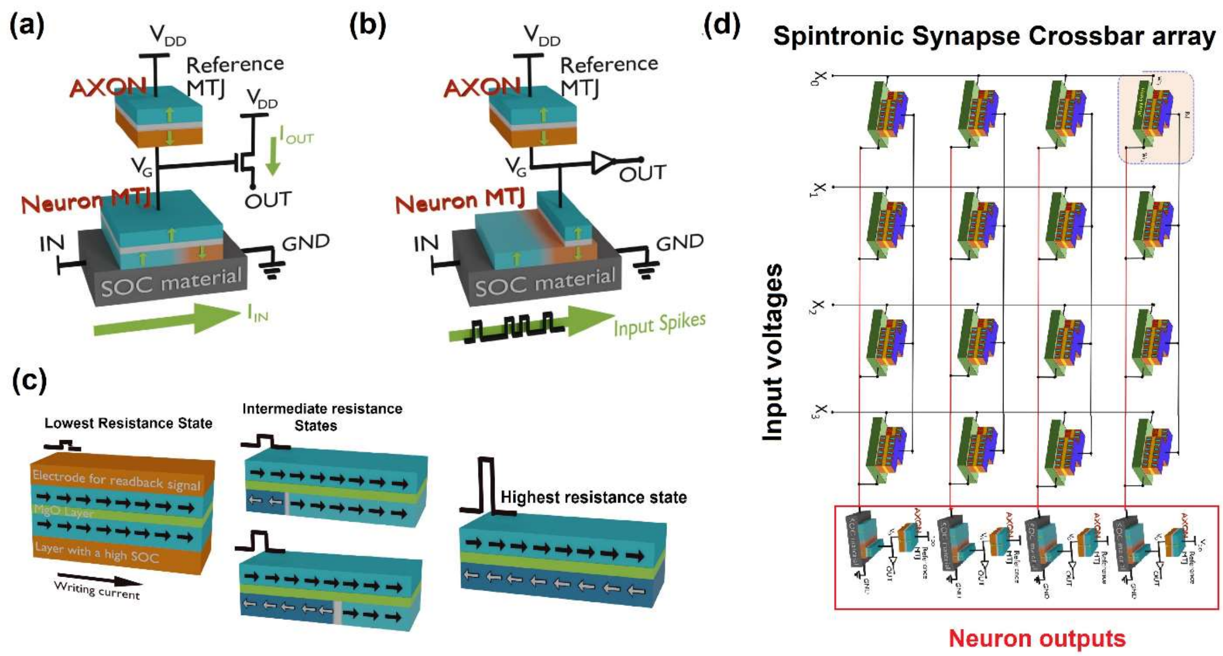

Figure 14. Illustration of DW MTJ-based neurons and synapses: (a) A step neuron is a domain wall based magnetic tunnel junction device. The output is analog like and the value depends on the position of the domain wall. (b) A spike neuron has the reference layer of a magnetic tunnel junction at one end of the domain wall device. The output is generated only when the domain wall reaches the region below the reference layer. (c) A domain wall device that exhibits multiple resistance states may be used for achieving synapse. The resistance of the device depends on the domain wall position. The position at which the domain wall gets pinned is determined by the pinning strategies used and the current pulses the synapse receives. (d) An all-spin neuromorphic processing element proposed by Sengupta and Roy [112].

Figure 14 shows different configurations of neurons and synapses that can be fabricated using domain wall based magnetic tunnel junctions. While there are various possibilities for neurons, two types of neurons are commonly investigated. In a "step neuron", the neuron receives inputs from other neurons and its value keeps changing as a function of received inputs. Such a step neuron can be fabricated using the design shown in Figure 14(a). In this design, the tunnel barrier and the reference layer are present throughout the domain wall device and the entire device is a magnetic tunnel junction. As a result, the domain wall position determines the magnetoresistance. Since the position of the domain wall changes gradually, the output increases in an analog manner.

Figure 14(b) shows a spike neuron, analogous to the neurons in the brain – which emits a spike when a critical potential is reached. The domain wall device which constitutes a spike neuron is mostly the free layer. The tunnel barrier and the reference layer are placed at one end only. As a consequence of such a design, the output of the spike neuron does not change much when the domain wall moves from one end to the other. However, when the domain wall reaches the region below the tunnel barrier and the reference layer, the output is changed resulting in a spike.

Figure 14(c) shows the concept of a domain wall MTJ-based synapse. Like step neuron, a synapse is also built by making the entire domain wall device as a magnetic tunnel junction. As a result, a synapse will exhibit multiple resistance states, depending on the position of the domain wall. To achieve clear steps in the multilevel resistance values, pinning techniques might be employed. The group of Piramanayagam et al., have investigated various techniques to pin the domain walls [89,135,140,141,143,257,258]

Neuromorphic computing circuits based on synapses and spike neurons have also been proposed. Figure 14(d) shows an all-spin neuromorphic processing element, proposed by Sengupta et al [112]. In this circuit, the synapses receive input voltages from other neurons. Depending on the conductivity of the synapse (which depends on the position of domain wall), the currents are added in the vertical column. Since the vertical column is connected to a neuron at the bottom, the neuron fires if the summation exceeds a critical value.

Powered by the simultaneously coexisting function of neurons and synapses with spintronic devices, all-spin neuromorphic computing has been proposed. Three algorithms, spiking neural networks (SNNs), reservoir computing and probabilistic computing, have received significant attention.

SNN works with discrete spiking trains. Spatio-temporal information of input data is encoded into spiking trains. In an SNN architecture, the action potential of neurons changes according to the LIF model, while synapses update their scaling weight according to some learning rules, such as the STDP rule. This bio-realistic SNN model tracks the initialization and propagation of action potentials in neurons and adjusts the synapse weight according to local spatio-temporal information. These features offer SNN advantages in processing dynamic systems like speech and gesture recognition, as well as real-world sensory data. The discrete and sparse nature of SNN enables powerful and energy-efficient neuromorphic computation [259]. Furthermore, with temporal information encoded, the performance of SNN is more robust to noise. Magnetic dynamics in a MTJ/HM crossbar array has been explored for SNNs [260]. In this work, thermally stochastic switching of MTJs mimic the probabilistic spiking of neurons and the stochastic-STDP learning rule is realized by the plasticity function of MTJ synapses. By simulation, MNIST classification with 74% accuracy was obtained [98]. To improve the MNIST classification accuracy, Wu et al. designed an all-spin SNN using back-hopping oscillation (BHO) in STT-MRAM [261]. The coupled local Joule heating and STT effects contribute to the bias-dependent BHO and the resulting Poisson neurons that encode information in the tunable duty cycle of probabilistic spiking trains. Using the all-spin SNN, their simulation achieved 98.4% accuracy for MNIST classification with at least 6x smaller chip area than the state-of-the-art integrate-and-fire (IF) CMOS neurons.

Reservoir computing maps input signals into desired outputs through the dynamic of a nonlinear reservoir system [262]. Generally, the reservoir system is fixed, and only the output layer is trainable. Therefore, reservoir computing has significant advantages in lower training cost and faster learning. Exploiting ultrafast nonlinear magnetic dynamics, reservoir computing on spintronic devices has been reported [150,263–267]. Based on micromagnetic simulation, Jiang et al. [265] investigated two reservoir computing systems using spin-torque nano-oscillators (STNOs) and a single magnetic skyrmion memristor (MSM), as shown in Figure 15(a). STNOs and MSM show nonlinear responses to current pulses. They achieved 87.7% accuracy on MNIST classification using a single MSM. Moreover, a complex task (NARMA10) with unknown nonlinear dynamic problems can be solved by STNOs. In addition, reservoir computing can be realized with nonlinear current-voltage response of skyrmions due to the non-crystalline anisotropic magneto-resistive effect. The anisotropic scattering of carriers by skyrmions leads to the magnetization dependent magnetoresistive effect. Therefore, non-crystalline anisotropic magnetoresistive effect can be achieved by controlling the type, shape, relative size and position of the skyrmion embedded in ferromagnetic thin films. When currents flow through skyrmions, tuning spin-orbit coupling and spin torque can deform, stretch, or even move the skyrmion in the ferromagnetic films. Furthermore, multiple skyrmions can be connected and arranged into a random, self-assembled, recursively connected configuration. The resulting skyrmion network can work for complex reservoir computing with excellent energy efficiency, adaptable and homeostatic operation.

Binary stochastic MTJs enable an emerging unconventional computing paradigm that is probabilistic computing [71,268–271], shown in Figure 15(b). The magnetization of an MTJ with low thermal barrier (~ kBT) shows random switching between 0 and 1 under thermal activation. A current induced spin-transfer torque or spin-orbit torque can tune the stochastic switching. Consequently, the input current and the probability of output (0, 1) states exhibit a sigmoidal activation function, which imitates the binary stochastic neuron in stochastic neural networks. Stochastic neural networks using binary SMTJs has been applied for modelling restricted Boltzmann machine, implementing Bayesian inference, simulating invertible Boolean logic, solving annealing optimization for quantum many-body Hamiltonians [272,273].

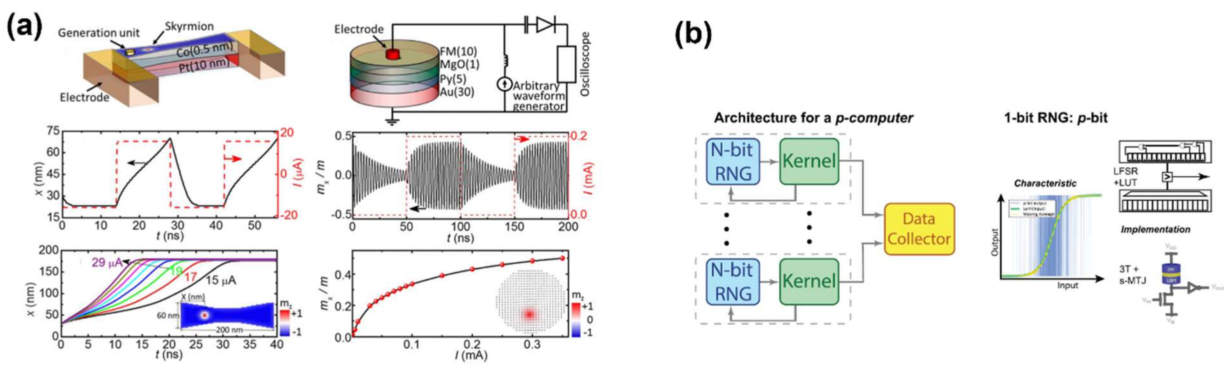

Figure 15. (a) Reservoir computing with skyrmions, showing schematic of a magnetic skyrmion memristor consisting of the dumbbell shape ferromagnetic Pt(10)/Co(0.5) bilayer; The skyrmion position (the black curve) under the stimulation of square current pulses (the red curve); Time dependent position of the centroid of the skyrmion at different currents; Schematic circuit with a vortex-type spin-torque nano-oscillators (STNO); The response of mx to the square current pulse, and the maximum envelope of mx /m procession motion at steady state as a function of the input current I. (Inset shows the snapshot of the instantaneous magnetization distribution of the STNO) [265]. (b) Schematic architecture of a probabilistic computer with a probabilistic element (N-bit RNG), deterministic elements (kernel and data collector), and the N-bit RNG block is a collection of p-bits. The input–output characteristics of p-bit can be realized by CMOS technology using linear feedback shift registers (LFSRs) and lookup tables (LUTs), or stochastic magnetic tunnel junction (s-MTJ) [271].

To summarize, the unique features of spintronic devices, including non-volatile, plastic, oscillatory and stochastic, offer them great flexibility to design neuromorphic neurons and synapses. This may pave the way to neuromorphic chips with ultrafast computing and extremely low power consumption.

VIII. CONCLUSIONS

The advance in AI technology raises requirements for enormous data storage and information processing. Searching for new AI architectures capable of high density and low power consumption is becoming imperative and challenging. Spintronic devices, with the advantages of non-volatility and low-power consumptions, have attracted immense attention. We have provided a systematic review of multistate nonvolatile spintronic devices towards high-density memory and neuromorphic computing, focusing on material and device structure concept designs. Multi-state in spintronic devices is achievable through various device concepts, such as domain wall motion in nanowires, domain nucleation in thin film structures, multilevel cells in series or parallel MTJs, free layers with multi-crossing ellipses, free layers with antiferromagnets, as well as assistance with other mechanisms, including electric field manipulated switching in PMN-PT heterostructures and resistance enhanced MTJs.

While utilizing the concept of magnetic domain wall motion and domain nucleation are natural paths to achieve multi-state spintronic devices, they are vulnerable to pinning by various defects, and generally only achieved in relatively large devices (order of several microns). Various schemes have been proposed to resolve the domain pinning issues, such as fabricating complex geometries or introducing process modifications e.g. ion-beam irradiation.

Multi-state switching in a single nanoscale ferromagnetic layer is a promising scheme for its simple geometry designs and small device sizes. This has recently been demonstrated using STT induced switching for p-MTJ or SOT induced switching for i-MTJ. However, studies on multi-state switching for nanoscale p-MTJ devices with three-terminal SOT mechanism is still lacking. We hence performed micromagnetic simulations to explore SOT-induced switching dynamics in nanoscale p-MTJs. We showed that stable intermediate magnetization states are achievable by controlling different pulse amplitudes under external magnetic fields for a circular free layer with a diameter of 1000 nm. Furthermore, field-free multistate switching can be achieved by exchange-coupling the perpendicular free layer to an in-plane magnetic layer having an elliptic shape, with the long axis oriented along the charge current direction.

Finally, the rich features of spintronic devices, including their non-volatile, plastic, oscillatory and stochastic characteristics are discussed. These unique features offer great flexibility to design neuromorphic neurons and synapses and may pave the way to neuromorphic chips with ultrafast computing and extremely low power consumption.

ACKNOWLEDGMENTS

This work is supported by Agency for Science, Technology and Research (A*STAR) under RIE2020 AME Programmatic Grant (Grant No. A18A6b0057), and Career Development Fund (Project No. C210812054). SNP gratefully acknowledges the funding from the National Research Foundation (NRF), Singapore for the CRP21 grant (NRF-CRP21-2018-0003).

DATA AVAILABILITY

The data that support the findings of this study are available from the corresponding author upon request.

REFERENCES

[1] S.N. Piramanayagam, J. Appl. Phys. 102 (2007) 011301.

[2] S.S.P. Parkin, in: Annu. Rev. Mater. Sci., Annual Reviews, 1995, pp. 357–388.

[3] S.S.P. Parkin, in: S. Maekawa, T. Shinjo (Eds.), Spin Depend. Transp. Magn. Nanostructures, Taylor & Francis, London, 2002.

[4] M.N. Baibich, J.M. Broto, A. Fert, F.N. Van Dau, F. Petroff, P. Eitenne, G. Creuzet, A. Friederich, J. Chazelas, Phys. Rev. Lett. 61 (1988) 2472–2475.

[5] G. Binasch, P. Grünberg, F. Saurenbach, W. Zinn, Phys. Rev. B 39 (1989) 4828–4830.

[6] M. Julliere, Phys. Lett. A 54 (1975) 225–226.

[7] T. Miyazaki, N. Tezuka, J. Magn. Magn. Mater. 139 (1995) L213.

[8] J.S. Moodera, L.R. Kinder, T.M. Wong, R. Meservey, Phys. Rev. Lett. 74 (1995) 3273–3276.

[9] S. Bhatti, R. Sbiaa, A. Hirohata, H. Ohno, S. Fukami, S.N. Piramanayagam, Mater. Today (2017).

[10] J. Åkerman, Science (80-.). 308 (2005) 508–510.

[11] A. V. Khvalkovskiy, D. Apalkov, S. Watts, R. Chepulskii, R.S. Beach, A. Ong, X. Tang, A.

Driskill-Smith, W.H. Butler, P.B. Visscher, D. Lottis, E. Chen, V. Nikitin, M. Krounbi, J. Phys. D. Appl. Phys. 46 (2013) 074001.

[12] M. Natsui, A. Tamakoshi, H. Honjo, T. Watanabe, T. Nasuno, C. Zhang, T. Tanigawa, H. Inoue, M. Niwa, T. Yoshiduka, Y. Noguchi, M. Yasuhira, Y. Ma, H. Shen, S. Fukami, H. Sato, S. Ikeda, H. Ohno, T. Endoh, T. Hanyu, IEEE J. Solid-State Circuits 56 (2021) 1116–1128.

[13] S.S.P. Parkin, K.P. Roche, M.G. Samant, P.M. Rice, R.B. Beyers, R.E. Scheuerlein, E.J. O'Sullivan, S.L. Brown, J. Bucchigano, D.W. Abraham, Y. Lu, M. Rooks, P.L. Trouilloud, R.A. Wanner, W.J. Gallagher, J. Appl. Phys. 85 (1999) 5828–5833.

[14] F. Zahoor, T.Z. Azni Zulkifli, F.A. Khanday, Nanoscale Res. Lett. 15 (2020) 90.

[15] M. Le Gallo, A. Sebastian, J. Phys. D. Appl. Phys. 53 (2020) 213002.

[16] H. Kohlstedt, Y. Mustafa, A. Gerber, A. Petraru, M. Fitsilis, R. Meyer, U. Böttger, R. Waser, Microelectron. Eng. 80 (2005) 296–304.

[17] W.H. Butler, X.G. Zhang, T.C. Schulthess, J.M. MacLaren, Phys. Rev. B - Condens. Matter Mater. Phys. 63 (2001) 544161–5441612.

[18] J. Mathon, A. Umerski, Phys. Rev. B - Condens. Matter Mater. Phys. 63 (2001) 1–4.

[19] S.S.P. Parkin, C. Kaiser, A. Panchula, P.M. Rice, B. Hughes, M. Samant, S.H. Yang, Nat. Mater. 3 (2004) 862–867.

[20] S. Yuasa, T. Nagahama, A. Fukushima, Y. Suzuki, K. Ando, Nat. Mater. 3 (2004) 868–871.

[21] P.G. Mather, J.C. Read, R.A. Buhrman, Phys. Rev. B - Condens. Matter Mater. Phys. 73 (2006) 1–5.

[22] W.H. Butler, Sci. Technol. Adv. Mater. 9 (2008) 014106.

[23] S. Tehrani, J.M. Slaughter, M. DeHerrera, B.N. Engel, N.D. Rizzo, J. Salter, M. Durlam, R.W. Dave, J. Janesky, B. Butcher, K. Smith, G. Grynkewich, Proc. IEEE 91 (2003) 703–712.

[24] J.C. Slonczewski, J. Magn. Magn. Mater. 159 (1996) L1–L7.

[25] L. Berger, Phys. Rev. B - Condens. Matter Mater. Phys. 54 (1996) 9353.

[26] I.M. Miron, K. Garello, G. Gaudin, P.J. Zermatten, M. V. Costache, S. Auffret, S. Bandiera, B. Rodmacq, A. Schuhl, P. Gambardella, Nature 476 (2011) 189–193.

[27] T. Jungwirth, J. Wunderlich, K. Olejník, Nat. Mater. 11 (2012) 382–390.

[28] L. Liu, C.F. Pai, Y. Li, H.W. Tseng, D.C. Ralph, R.A. Buhrman, Science (80-.). 336 (2012) 555–558.

[29] S. Fukami, T. Anekawa, C. Zhang, H. Ohno, Nat. Nanotechnol. 11 (2016) 621–625.

[30] C.F. Pai, L. Liu, Y. Li, H.W. Tseng, D.C. Ralph, R.A. Buhrman, Appl. Phys. Lett. 101 (2012) 122404.

[31] L. Liu, O.J. Lee, T.J. Gudmundsen, D.C. Ralph, R.A. Buhrman, Phys. Rev. Lett. 109 (2012)

096602.
[32] A.R. Mellnik, J.S. Lee, A. Richardella, J.L. Grab, P.J. Mintun, M.H. Fischer, A. Vaezi, A. Manchon, E.A. Kim, N. Samarth, D.C. Ralph, Nature 511 (2014) 449.
[33] S. Ikeda, K. Miura, H. Yamamoto, K. Mizunuma, H.D. Gan, M. Endo, S. Kanai, J. Hayakawa, F. Matsukura, H. Ohno, Nat. Mater. 9 (2010) 721–724.
[34] H. Liu, D. Bedau, D. Backes, J.A. Katine, J. Langer, A.D. Kent, Appl. Phys. Lett. 97 (2010) 242510.
[35] K. Garello, C.O. Avci, I.M. Miron, M. Baumgartner, A. Ghosh, S. Auffret, O. Boulle, G. Gaudin, P. Gambardella, Appl. Phys. Lett. 105 (2014) 212402.
[36] C. Pan, A. Naeemi, IEEE J. Explor. Solid-State Comput. Devices Circuits 3 (2017) 10–17.
[37] Y. Kim, X. Fong, K.W. Kwon, M.C. Chen, K. Roy, IEEE Trans. Electron Devices 62 (2015) 561–568.
[38] X. Fong, Y. Kim, R. Venkatesan, S.H. Choday, A. Raghunathan, K. Roy, Proc. IEEE 104 (2016) 1449–1488.
[39] Q. Cao, W. Lü, X.R. Wang, X. Guan, L. Wang, S. Yan, T. Wu, X. Wang, ACS Appl. Mater. Interfaces 12 (2020) 42449–42471.
[40] R. Sbiaa, Phys. Status Solidi - Rapid Res. Lett. 15 (2021) 1–9.
[41] C. Wang, A. Agrawal, E. Yu, K. Roy, Front. Neurosci. 15 (2021) 1–19.
[42] G. Indiveri, E. Chicca, R. Douglas, IEEE Trans. Neural Networks 17 (2006) 211–221.
[43] J. von Neumann, IEEE Ann. Hist. Comput. 15 (1993) 27–75.
[44] N. Mahapatra, B. Venkatrao, XRDS Crossroads, ACM Mag. Students 5 (1999) 2.
[45] M.D. Hill, Aspects of Cache Memory and Instruction Buffer Performance, 1987.
[46] M. Versace, B. Chandler, IEEE Spectr. 47 (2010) 30–37.
[47] W.S. Mcculloch, W. Pitts, Bull. Math. Biol. 52 (1990) 99–115.
[48] L. Chua, IEEE Trans. Circuit Theory 18 (1971) 507–519.
[49] D.B. Strukov, G.S. Snider, D.R. Stewart, R.S. Williams, Nature 453 (2008) 80–83.
[50] J.J. Yang, M.D. Pickett, X. Li, D.A.A. Ohlberg, D.R. Stewart, R.S. Williams, Nat. Nanotechnol. 3 (2008) 429–433.
[51] S.H. Jo, T. Chang, I. Ebong, B.B. Bhadviya, P. Mazumder, W. Lu, Nano Lett. 10 (2010) 1297–1301.
[52] T. Prodromakis, C. Toumazou, L. Chua, Nat. Mater. 11 (2012) 478–481.
[53] Y. Watanabe, J.G. Bednorz, A. Bietsch, C. Gerber, D. Widmer, A. Beck, S.J. Wind, Appl. Phys. Lett. 78 (2001) 3738–3740.
[54] R. Waser, M. Aono, Nat. Mater. 6 (2007) 833–840.

[55] D.S. Jeong, R. Thomas, R.S. Katiyar, J.F. Scott, H. Kohlstedt, A. Petraru, C.S. Hwang, Reports Prog. Phys. 75 (2012) 076502.
[56] D. Kuzum, S. Yu, H.S. Philip Wong, Nanotechnology 24 (2013) 382001.
[57] S.W. Fong, C.M. Neumann, H.P. Wong, EEE Trans. Electron Devices 64 (2017) 4374–4385.
[58] L. Wang, S.R. Lu, J. Wen, Nanoscale Res. Lett. 12 (2017) 347.
[59] H.S.P. Wong, S. Raoux, S. Kim, J. Liang, J.P. Reifenberg, B. Rajendran, M. Asheghi, K.E. Goodson, Proc. IEEE 98 (2010) 2201–2227.
[60] J. Grollier, D. Querlioz, M.D. Stiles, Proc. IEEE 104 (2016) 2024–2039.
[61] E. Chen, D. Apalkov, A. Driskill-Smith, A. Khvalkovskiy, D. Lottis, K. Moon, V. Nikitin, A. Ong, X. Tang, S. Watts, R. Kawakami, M. Krounbi, S.A. Wolf, S.J. Poon, J.W. Lu, A.W. Ghosh, M. Stan, W. Butler, T. Mewes, S. Gupta, C.K.A. Mewes, P.B. Visscher, R.A. Lukaszew, IEEE Trans. Magn. 48 (2012) 3025–3030.
[62] T. Na, S.H. Kang, S.-O. Jung, IEEE Trans. CIRCUITS Syst. EXPRESS BRIEFS 68 (2021) 12–18.
[63] S.J. Lin, Y.L. Huang, M.Y. Song, C.M. Lee, F. Xue, G.L. Chen, S.Y. Yang, Y.J. Chang, I.J. Wang, Y.C. Hsin, Y.H. Su, J.H. Wei, C.F. Pai, S.X. Wang, C.H. Diaz, IEEE Int. Reliab. Phys. Symp. Proc. March 2021 (2021) 12–14.
[64] M. Sharad, D. Fan, K. Roy, J. Appl. Phys. 114 (2013).
[65] A. Sengupta, S.H. Choday, Y. Kim, K. Roy, Appl. Phys. Lett. 106 (2015) 143701.
[66] K. Hayakawa, S. Kanai, T. Funatsu, J. Igarashi, B. Jinnai, W.A. Borders, H. Ohno, S. Fukami, Phys. Rev. Lett. 126 (2021) 117202.
[67] K. Kobayashi, W.A. Borders, S. Kanai, K. Hayakawa, H. Ohno, S. Fukami, Appl. Phys. Lett. 119 (2021) 132406.
[68] A. Sengupta, P. Panda, P. Wijesinghe, Y. Kim, K. Roy, Sci. Rep. 6 (2016) 1–9.
[69] K. Yogendra, D. Fan, B. Jung, K. Roy, IEEE Trans. Electron Devices 63 (2016) 1674–1680.
[70] A.A. Awad, P. Dürrenfeld, A. Houshang, M. Dvornik, E. Iacocca, R.K. Dumas, J. Åkerman, Nat. Phys. 13 (2017) 292–299.
[71] K.Y. Camsari, S. Salahuddin, S. Datta, IEEE Electron Device Lett. 38 (2017) 1767–1770.
[72] J. Torrejon, M. Riou, F.A. Araujo, S. Tsunegi, G. Khalsa, D. Querlioz, P. Bortolotti, V. Cros, K. Yakushiji, A. Fukushima, H. Kubota, S. Yuasa, M.D. Stiles, J. Grollier, Nature 547 (2017) 428–431.
[73] A. Kurenkov, S. DuttaGupta, C. Zhang, S. Fukami, Y. Horio, H. Ohno, Adv. Mater. 31 (2019) 1900636.
[74] A. Sengupta, G. Srinivasan, D. Roy, K. Roy, Tech. Dig. - Int. Electron Devices Meet. IEDM 2018-Decem (2019) 15.6.1-15.6.4.

[75] D.W. Kim, W.S. Yi, J.Y. Choi, K. Ashiba, J.U. Baek, H.S. Jun, J.J. Kim, J.G. Park, Front. Neurosci. 14 (2020) 1–9.

[76] W. Senn, S. Fusi, Phys. Rev. E - Stat. Nonlinear, Soft Matter Phys. 71 (2005) 1–12.

[77] M. Sharad, C. Augustine, G. Panagopoulos, K. Roy, IEEE Trans. Nanotechnol. 11 (2012) 843–853.

[78] J. Bill, R. Legenstein, Front. Neurosci. 8 (2014) 1–18.

[79] A.F. Vincent, J. Larroque, N. Locatelli, N. Ben Romdhane, O. Bichler, C. Gamrat, W.S. Zhao, J.O. Klein, S. Galdin-Retailleau, D. Querlioz, IEEE Trans. Biomed. Circuits Syst. 9 (2015) 166–174.

[80] S. Fukami, C. Zhang, S. Duttagupta, A. Kurenkov, H. Ohno, Nat. Mater. 15 (2016) 535–542.

[81] S. Lequeux, J. Sampaio, V. Cros, K. Yakushiji, A. Fukushima, R. Matsumoto, H. Kubota, S. Yuasa, J. Grollier, Sci. Rep. 6 (2016) 1–7.

[82] D. Zhang, L. Zeng, K. Cao, M. Wang, S. Peng, Y. Zhang, Y. Zhang, J.O. Klein, Y. Wang, W. Zhao, IEEE Trans. Biomed. Circuits Syst. 10 (2016) 828–836.

[83] W.A. Borders, H. Akima, S. Fukami, S. Moriya, S. Kurihara, Y. Horio, S. Sato, H. Ohno, Appl. Phys. Express 10 (2017) 013007.

[84] N. Locatelli, A.F. Vincent, D. Querlioz, 2018 25th IEEE Int. Conf. Electron. Circuits Syst. ICECS 2018 (2019) 553–556.

[85] A. Basu, J. Acharya, T. Karnik, H. Liu, H. Li, J.S. Seo, C. Song, IEEE J. Emerg. Sel. Top. Circuits Syst. 8 (2018) 6–27.

[86] J. Grollier, D. Querlioz, K.Y. Camsari, K. Everschor-Sitte, S. Fukami, M.D. Stiles, Nat. Electron. 3 (2020) 360–370.

[87] H. Sato, M. Yamanouchi, S. Ikeda, S. Fukami, F. Matsukura, H. Ohno, Appl. Phys. Lett. 101 (2012) 022414.

[88] H. Sato, M. Yamanouchi, K. Miura, S. Ikeda, H.D. Gan, K. Mizunuma, R. Koizumi, F. Matsukura, H. Ohno, Appl. Phys. Lett. 99 (2011) 042501.

[89] D. Kumar, T. Jin, R. Sbiaa, M. Kläui, S. Bedanta, S. Fukami, D. Ravelosona, S.H. Yang, X. Liu, S.N. Piramanayagam, Phys. Rep. 958 (2022) 1–35.

[90] A. Sengupta, Y. Shim, K. Roy, IEEE Trans. Biomed. Circuits Syst. 10 (2016) 1152–1160.

[91] C.K. Lim, T. Devolder, C. Chappert, J. Grollier, V. Cros, A. Vaurès, A. Fert, G. Faini, Appl. Phys. Lett. 84 (2004) 2820–2822.

[92] Z. He, D. Fan, IEEE Trans. Emerg. Top. Comput. 5 (2017) 223–237.

[93] X. Wang, Y. Chen, H. Xi, H. Li, D. Dimitrov, IEEE Electron Device Lett. 30 (2009) 294–297.

[94] R. Sbiaa, S.N. Piramanayagam, Appl. Phys. A Mater. Sci. Process. 114 (2014) 1347–1351.

[95] M. Al Bahri, J. Magn. Magn. Mater. 543 (2022) 168611.
[96] A. Sengupta, Z. Al Azim, X. Fong, K. Roy, Appl. Phys. Lett. 106 (2015) 093704.
[97] S. Emori, U. Bauer, S.M. Ahn, E. Martinez, G.S.D. Beach, Nat. Mater. 12 (2013) 611–616.
[98] G. Srinivasan, A. Sengupta, K. Roy, Sci. Rep. 6 (2016) 1–13.
[99] A. Sengupta, K. Roy, Appl. Phys. Rev. 4 (2017) 041105.
[100] Y. Liu, B. Zhou, J.G. (Jimmy) Zhu, Sci. Rep. 9 (2019) 325.
[101] D. Bhowmik, U. Saxena, A. Dankar, A. Verma, D. Kaushik, S. Chatterjee, U. Singh, J. Magn. Magn. Mater. 489 (2019) 165434.
[102] K. Yue, Y. Liu, R.K. Lake, A.C. Parker, Sci. Adv. 5 (2019) 1–10.
[103] E. Raymenants, O. Bultynck, D. Wan, T. Devolder, K. Garello, L. Souriau, A. Thiam, D. Tsvetanova, Y. Canvel, D.E. Nikonov, I.A. Young, M. Heyns, B. Soree, I. Asselberghs, I. Radu, S. Couet, V.D. Nguyen, Nat. Electron. 4 (2021) 392–398.
[104] T. Moriya, Phys. Rev. Lett. 4 (1960) 228–230.
[105] A. Thiaville, S. Rohart, É. Jué, V. Cros, A. Fert, Epl 100 (2012) 57002.
[106] K.S. Ryu, L. Thomas, S.H. Yang, S. Parkin, Nat. Nanotechnol. 8 (2013) 527–533.
[107] W. Legrand, J.Y. Chauleau, D. Maccariello, N. Reyren, S. Collin, K. Bouzehouane, N. Jaouen, V. Cros, A. Fert, Sci. Adv. 4 (2018) 1–10.
[108] X. Zhang, W. Cai, X. Zhang, Z. Wang, Z. Li, Y. Zhang, K. Cao, N. Lei, W. Kang, Y. Zhang, H. Yu, Y. Zhou, W. Zhao, ACS Appl. Mater. Interfaces 10 (2018) 16887–16892.
[109] S. Fukami, M. Yamanouchi, S. Ikeda, H. Ohno, IEEE Trans. Magn. 50 (2014) 3401006.
[110] Y. Seo, K.W. Kwon, K. Roy, IEEE Electron Device Lett. 37 (2016) 982–985.
[111] B. Chen, Domain Wall Motion in a Perpendicular Magnetized Nanowire, n.d.
[112] A. Sengupta, K. Roy, IEEE Trans. Circuits Syst. I Regul. Pap. 63 (2016) 2267–2277.
[113] X. Zhao, B. Zhang, N. Vernier, X. Zhang, M. Sall, T. Xing, L.H. Diez, C. Hepburn, L. Wang, G. Durin, A. Casiraghi, M. Belmeguenai, Y. Roussigné, A. Stashkevich, S.M. Chérif, J. Langer, B. Ocker, S. Jaiswal, G. Jakob, M. Kläui, W. Zhao, D. Ravelosona, Appl. Phys. Lett. 115 (2019).
[114] D. Wan, M. Manfrini, A. Vaysset, L. Souriau, L. Wouters, A. Thiam, E. Raymenants, S. Sayan, J. Jussot, J. Swerts, S. Couet, N. Rassoul, K.B. Gavan, K. Paredis, C. Huyghebaert, M. Ercken, C.J. Wilson, D. Mocuta, I.P. Radu, Jpn. J. Appl. Phys. 57 (2018) 04FN01.
[115] S.H. Yang, K.S. Ryu, S. Parkin, Nat. Nanotechnol. 10 (2015) 221–226.
[116] Y.U. Kim, J. Kwon, H.K. Hwang, I. Purnama, C.Y. You, Sci. Rep. 10 (2020) 1–9.
[117] S. Liu, T.P. Xiao, C. Cui, J.A.C. Incorvia, C.H. Bennett, M.J. Marinella, Appl. Phys. Lett. 118 (2021) 202405.
[118] G.S.D. Beach, C. Nistor, C. Knutson, M. Tsoi, J.L. Erskine, Nat. Mater. 4 (2005) 741–744.

[119] L.K. Bogart, D. Atkinson, K. O'Shea, D. McGrouther, S. McVitie, Phys. Rev. B - Condens. Matter Mater. Phys. 79 (2009) 1–8.
[120] U. Bauer, S. Emori, G.S.D. Beach, Nat. Nanotechnol. 8 (2013) 411–416.
[121] D. Castilla, M. Maicas, J.L. Prieto, M.P. Proenca, J. Phys. D. Appl. Phys. 50 (2017) 105001.
[122] Y. Gao, B. You, X.Z. Ruan, M.Y. Liu, H.L. Yang, Q.F. Zhan, Z. Li, N. Lei, W.S. Zhao, D.F. Pan, J.G. Wan, J. Wu, H.Q. Tu, J. Wang, W. Zhang, Y.B. Xu, J. Du, Sci. Rep. 6 (2016) 1–8.
[123] S.H. Huang, C.H. Lai, Appl. Phys. Lett. 95 (2009) 1–4.
[124] M. Kläui, H. Ehrke, U. Rüdiger, T. Kasama, R.E. Dunin-Borkowski, D. Backes, L.J. Heyderman, C.A.F. Vaz, J.A.C. Bland, G. Faini, E. Cambril, W. Wernsdorfer, Appl. Phys. Lett. 87 (2005) 1–4.
[125] D. Petit, A.V. Jausovec, D. Read, R.P. Cowburn, J. Appl. Phys. 103 (2008) 114307.
[126] K. Xu, D.K. Schreiber, Y. Li, B.R. Johnson, J. McCloy, AIP Adv. 7 (2017) 056806.
[127] M. Al Bahri, R. Sbiaa, Sci. Rep. 6 (2016) 1–8.
[128] R. Sbiaa, M. Al Bahri, J. Magn. Magn. Mater. 411 (2016) 113–115.
[129] M. Al Bahri, B. Borie, T.L. Jin, R. Sbiaa, M. Kläui, S.N. Piramanayagam, Phys. Rev. Appl. 11 (2019) 1.
[130] H. Mohammed, S. Al Risi, T.L. Jin, J. Kosel, S.N. Piramanayagam, R. Sbiaa, Appl. Phys. Lett. 116 (2020).
[131] J. Cai, B. Fang, C. Wang, Z. Zeng, Appl. Phys. Lett. 111 (2017) 1–5.
[132] M. Hayashi, L. Thomas, C. Rettner, R. Moriya, X. Jiang, S.S.P. Parkin, Phys. Rev. Lett. 97 (2006) 1–4.
[133] O. Akinola, X. Hu, C.H. Bennett, M. Marinella, J.S. Friedman, J.A.C. Incorvia, J. Phys. D. Appl. Phys. 52 (2019).
[134] M.A. Azam, D. Bhattacharya, D. Querlioz, C.A. Ross, J. Atulasimha, Nanotechnology 31 (2020).
[135] T. Jin, F. Tan, C.C. Ang, C. Gan, J. Cao, W. Lew, S. Piramanayagam, in: IEEE Int. Magn. Conf. (INTERMAG), Apr 23-27; Singapore, 2018.
[136] I. Polenciuc, A.J. Vick, D.A. Allwood, T.J. Hayward, G. Vallejo-Fernandez, K. O'Grady, A. Hirohata, Appl. Phys. Lett. 105 (2014) 162406.
[137] T. Jin, W. Gan, F. Tan, N.R. Sernicola, W.S. Lew, S.N. Piramanayagam, J. Phys. D. Appl. Phys. 52 (2019).
[138] Y.M. Hung, Y. Shiota, R. Hisatomi, T. Moriyama, T. Ono, Appl. Phys. Express 14 (2021) 023001.
[139] Y.M. Hung, T. Li, R. Hisatomi, Y. Shiota, T. Moriyama, T. Ono, J. Magn. Soc. Japan 45 (2021) 6–11.
[140] T. Jin, M. Ranjbar, S.K. He, W.C. Law, T.J. Zhou, W.S. Lew, X.X. Liu, S.N. Piramanayagam, Sci. Rep. 7 (2017) 1–9.

[141] T. Jin, D. Kumar, W. Gan, M. Ranjbar, F. Luo, R. Sbiaa, X. Liu, W.S. Lew, S.N. Piramanayagam, Phys. Status Solidi - Rapid Res. Lett. 12 (2018).

[142] M. Yang, Y. Li, J. Luo, Y. Deng, N. Zhang, X. Zhang, S. Li, Y. Cui, P. Yu, T. Yang, Y. Sheng, S. Wang, J. Xu, C. Zhao, K. Wang, Phys. Rev. Appl. 15 (2021) 1–8.

[143] D. Kumar, J. Chan, S.N. Piramanayagam, J. Appl. Phys. 130 (2021) 213901.

[144] J.M. Hu, T. Yang, K. Momeni, X. Cheng, L. Chen, S. Lei, S. Zhang, S. Trolier-Mckinstry, V. Gopalan, G.P. Carman, C.W. Nan, L.Q. Chen, Nano Lett. 16 (2016) 2341–2348.

[145] A. Chanthbouala, R. Matsumoto, J. Grollier, V. Cros, A. Anane, A. Fert, A. V. Khvalkovskiy, K.A. Zvezdin, K. Nishimura, Y. Nagamine, H. Maehara, K. Tsunekawa, A. Fukushima, S. Yuasa, Nat. Phys. 7 (2011) 626–630.

[146] M. Kläui, C.A.F. Vaz, J.A.C. Bland, W. Wernsdorfer, G. Faini, E. Cambril, L.J. Heyderman, F. Nolting, U. Rüdiger, Phys. Rev. Lett. 94 (2005) 106601.

[147] M. Hayashi, L. Thomas, C. Rettner, R. Moriya, Y.B. Bazaliy, S.S.P. Parkin, Phys. Rev. Lett. 98 (2007) 037204.

[148] C.H. Wan, M.E. Stebliy, X. Wang, G.Q. Yu, X.F. Han, A.G. Kolesnikov, M.A. Bazrov, M.E. Letushev, A. V. Ognev, A.S. Samardak, Appl. Phys. Lett. 118 (2021) 032407.

[149] J. Zhou, T. Zhao, X. Shu, L. Liu, W. Lin, S. Chen, S. Shi, X. Yan, X. Liu, J. Chen, Adv. Mater. 33 (2021).

[150] D. Prychynenko, M. Sitte, K. Litzius, B. Krüger, G. Bourianoff, M. Kläui, J. Sinova, K. Everschor-Sitte, Phys. Rev. Appl. 9 (2018) 14034.

[151] S. Li, W. Kang, Y. Huang, Zh. Xichao, Y. Zhou, W. Zhao, Nanotechnology 28 (2017) 31LT01.

[152] W. Kang, Y. Huang, X. Zhang, Y. Zhou, W. Zhao, Proc. IEEE 104 (2016) 2040–2061.

[153] A. Kurenkov, C. Zhang, S. DuttaGupta, S. Fukami, H. Ohno, Appl. Phys. Lett. 110 (2017) 092410.

[154] S. Fukami, H. Ohno, J. Appl. Phys. 124 (2018) 151904.

[155] P.H. Lin, B.Y. Yang, M.H. Tsai, P.C. Chen, K.F. Huang, H.H. Lin, C.H. Lai, Nat. Mater. 18 (2019) 335–341.

[156] X.H. Liu, K.W. Edmonds, Z.P. Zhou, K.Y. Wang, Phys. Rev. Appl. 13 (2020) 014059.

[157] T. Shibata, T. Shinohara, T. Ashida, M. Ohta, K. Ito, S. Yamada, Y. Terasaki, T. Sasaki, Appl. Phys. Express 13 (2020) 8–12.

[158] J. Yun, Q. Bai, Z. Yan, M. Chang, J. Mao, Y. Zuo, D. Yang, L. Xi, D. Xue, Adv. Funct. Mater. 30 (2020) 1909092.

[159] G.K. Krishnaswamy, A. Kurenkov, G. Sala, M. Baumgartner, V. Krizakova, C. Nistor, F. MacCherozzi, S.S. Dhesi, S. Fukami, H. Ohno, P. Gambardella, Phys. Rev. Appl. 14 (2020) 1.

[160] P. Dunne, C. Fowley, G. Hlawacek, J. Kurian, G. Atcheson, S. Colis, N. Teichert, B. Kundys, M. Venkatesan, J. Lindner, A.M. Deac, T.M. Hermans, J.M.D. Coey, B. Doudin, Nano Lett. 20 (2020) 7036–7042.

[161] X. Zhao, Y. Liu, D. Zhu, M. Sall, X. Zhang, H. Ma, J. Langer, B. Ocker, S. Jaiswal, G. Jakob, M. Kläui, W. Zhao, D. Ravelosona, Appl. Phys. Lett. 116 (2020) 242401.

[162] S. Zhang, Y. Su, X. Li, R. Li, W. Tian, J. Hong, L. You, Appl. Phys. Lett. 114 (2019) 042401.

[163] S. Zhang, S. Luo, N. Xu, Q. Zou, M. Song, J. Yun, Q. Luo, Z. Guo, R. Li, W. Tian, X. Li, H. Zhou, H. Chen, Y. Zhang, X. Yang, W. Jiang, K. Shen, J. Hong, Z. Yuan, L. Xi, K. Xia, S. Salahuddin, B. Dieny, L. You, Adv. Electron. Mater. 5 (2019) 1–7.

[164] K.F. Huang, D.S. Wang, M.H. Tsai, H.H. Lin, C.H. Lai, Adv. Mater. 29 (2017).

[165] G.J. Lim, W.L. Gan, W.C. Law, C. Murapaka, W.S. Lew, J. Magn. Magn. Mater. 514 (2020).

[166] Y. Sheng, Y.C. Li, X.Q. Ma, K.Y. Wang, Appl. Phys. Lett. 113 (2018) 112406.

[167] D. Li, B. Cui, X. Guo, Z. Xiao, W. Zhang, X. Jia, J. Duan, X. Liu, J. Chen, Z. Quan, G. Yu, X. Xu, APL Mater. 9 (2021) 1–5.

[168] Y. Cao, A.W. Rushforth, Y. Sheng, H. Zheng, K. Wang, Adv. Funct. Mater. 29 (2019) 1808104.

[169] Y. Yang, Y. Yang, H. Xie, Y. Xu, Z. Luo, Y. Wu, Phys. Rev. Appl. 13 (2020) 1.

[170] Y. Huang, W. Kang, X. Zhang, Y. Zhou, W. Zhao, Nanotechnology 28 (2017) 08LT02.

[171] M.C. Chen, A. Sengupta, K. Roy, IEEE Trans. Magn. 54 (2018) 1500207.

[172] X. Zhang, Y. Zhou, K.M. Song, T.E. Park, J. Xia, M. Ezawa, X. Liu, W. Zhao, G. Zhao, S. Woo, J. Phys. Condens. Matter 32 (2020).

[173] Y. Wang, L. Wang, J. Xia, Z. Lai, G. Tian, X. Zhang, Z. Hou, X. Gao, W. Mi, C. Feng, M. Zeng, G. Zhou, G. Yu, G. Wu, Y. Zhou, W. Wang, X. xiang Zhang, J. Liu, Nat. Commun. 11 (2020) 3577.

[174] S. Li, A. Du, Y. Wang, X. Wang, X. Zhang, H. Cheng, W. Cai, S. Lu, K. Cao, B. Pan, N. Lei, W. Kang, J. Liu, A. Fert, Z. Hou, W. Zhao, Sci. Bull. 67 (2022) 691–699.

[175] Y. Zhou, Natl. Sci. Rev. 6 (2019) 210–212.

[176] B. Göbel, I. Mertig, O.A. Tretiakov, Phys. Rep. 895 (2021) 1–28.

[177] S. Luo, L. You, APL Mater. 9 (2021) 050901.

[178] K. Everschor-Sitte, J. Masell, R.M. Reeve, M. Kläui, J. Appl. Phys. 124 (2018) 240901.

[179] H. Zhong, Y. Wen, Y. Zhao, Q. Zhang, Q. Huang, Y. Chen, J. Cai, X. Zhang, R. wei Li, L. Bai, S. Kang, S. Yan, Y. Tian, Adv. Funct. Mater. 29 (2019) 1–5.

[180] W.S. Zhao, Y. Zhang, T. Devolder, J.O. Klein, D. Ravelosona, C. Chappert, P. Mazoyer, Microelectron. Reliab. 52 (2012) 1848–1852.

[181] G. Prenat, K. Jabeur, P. Vanhauwaert, G. Di Pendina, F. Oboril, R. Bishnoi, M. Ebrahimi, N.

Lamard, O. Boulle, K. Garello, J. Langer, B. Ocker, M.C. Cyrille, P. Gambardella, M. Tahoori, G. Gaudin, IEEE Trans. Multi-Scale Comput. Syst. (2016).
[182] M. Cubukcu, O. Boulle, N. Mikuszeit, C. Hamelin, T. Bracher, N. Lamard, M.C. Cyrille, L. Buda-Prejbeanu, K. Garello, I.M. Miron, O. Klein, G. De Loubens, V. V. Naletov, J. Langer, B. Ocker, P. Gambardella, G. Gaudin, IEEE Trans. Magn. 54 (2018) 9300204.
[183] S. Prajapati, S. Verma, A.A. Kulkarni, B.K. Kaushik, IEEE Trans. Nanotechnol. 18 (2019) 1005–1014.
[184] P. Rzeszut, W. Skowroński, S. Ziętek, J. Wrona, T. Stobiecki, J. Appl. Phys. 125 (2019) 223907.
[185] P. Rzeszut, J. Chęciński, I. Brzozowski, S. Ziętek, W. Skowroński, T. Stobiecki, Sci. Rep. 12 (2022) 7178.
[186] A. Vatankhahghadim, A. Sheikholeslami, Proc. Int. Symp. Mult. Log. September (2015) 158–163.
[187] X. Lou, Z. Gao, D. V. Dimitrov, M.X. Tang, Appl. Phys. Lett. 93 (2008) 242502.
[188] T. Ishigaki, T. Kawahara, R. Takemura, K. Ono, K. Ito, H. Matsuoka, H. Ohno, Dig. Tech. Pap. - Symp. VLSI Technol. (2010) 47–48.
[189] G. Panagopoulos, C. Augustine, X. Fong, K. Roy, Device Res. Conf. - Conf. Dig. DRC (2012) 139–140.
[190] K. Tsunoda, M. Aoki, H. Noshiro, T. Takenaga, C. Yoshida, Y. Yamazaki, A. Takahashi, Y. Iba, A. Hatada, M. Nakabayashi, T. Sugii, Tech. Dig. - Int. Electron Devices Meet. IEDM 3 (2013) 64–67.
[191] M. Wang, S. Peng, Y. Zhang, Y. Zheng, Y. Zhang, Q. Zhang, D. Ravelosona, W. Zhao, IEEE Trans. Magn. 51 (2015) 12–15.
[192] R. Sbiaa, R. Law, S.Y.H. Lua, E.L. Tan, T. Tahmasebi, C.C. Wang, S.N. Piramanayagam, Appl. Phys. Lett. 99 (2011) 98–101.
[193] E. Raymenants, A. Vaysset, D. Wan, M. Manfrini, O. Zografos, O. Bultynck, J. Doevenspeck, M. Heyns, I.P. Radu, T. Devolder, J. Appl. Phys. 124 (2018) 152116.
[194] A. Nisar, S. Member, S. Dhull, S. Member, IEEE Trans. Electron Devices 68 (2021) 4384–4390.
[195] S. Fukami, T. Suzuki, K. Nagahara, N. Ohshima, Y. Ozaki, S. Saito, R. Nebashi, N. Sakimura, H. Honjo, K. Mori, C. Igarashi, S. Miura, N. Ishiwata, T. Sugibayashi, Dig. Tech. Pap. - Symp. VLSI Technol. (2009) 230–231.
[196] S. Fukami, M. Yamanouchi, K.J. Kim, T. Suzuki, N. Sakimura, D. Chiba, S. Ikeda, T. Sugibayashi, N. Kasai, T. Ono, H. Ohno, Tech. Dig. - Int. Electron Devices Meet. IEDM (2013) 72–75.
[197] M. Sharad, K. Roy, IEEE Electron Device Lett. 34 (2013) 1068–1070.
[198] M. Sharad, R. Venkatesan, A. Raghunathan, K. Roy, Proc. Int. Symp. Low Power Electron. Des.

(2013) 64–69.
[199] S.A. Siddiqui, S. Dutta, A. Tang, L. Liu, C.A. Ross, M.A. Baldo, Nano Lett. 20 (2020) 1033–1040.
[200] H.S. Jun, J.Y. Choi, K. Ashiba, S.H. Jung, M. Park, J.U. Baek, T.H. Shim, J.G. Park, AIP Adv. 10 (2020) 1–8.
[201] J.Y. Choi, H. Jun, K. Ashiba, J.U. Baek, T.H. Shim, J.G. Park, Sci. Rep. 9 (2019) 11932.
[202] J. Hong, M. Stone, B. Navarrete, K. Luongo, Q. Zheng, Z. Yuan, K. Xia, N. Xu, J. Bokor, L. You, S. Khizroev, Appl. Phys. Lett. 112 (2018) 112402.
[203] J. Hong, X. Li, N. Xu, H. Chen, S. Cabrini, S. Khizroev, J. Bokor, L. You, Adv. Intell. Syst. 2 (2020) 2000143.
[204] T. Maruyama, Y. Shiota, T. Nozaki, K. Ohta, N. Toda, M. Mizuguchi, A.A. Tulapurkar, T. Shinjo, M. Shiraishi, S. Mizukami, Y. Ando, Y. Suzuki, Nat. Nanotechnol. 4 (2009) 158–161.
[205] Y. Telepinsky, V. Mor, M. Schultz, Y.M. Hung, A.D. Kent, L. Klein, Appl. Phys. Lett. 108 (2016) 182401.
[206] S. Das, L. Avraham, Y. Telepinsky, V. Mor, M. Schultz, L. Klein, Sci. Rep. 8 (2018) 15160.
[207] S. Das, A. Zaig, H. Nhalil, L. Avraham, M. Schultz, L. Klein, Sci. Rep. 9 (2019) 20368.
[208] S. Das, A. Zaig, M. Schultz, S. Cardoso, D.C. Leitao, L. Klein, Appl. Phys. Lett. 117 (2020) 072404.
[209] S. Amara, U. Myrzakhan, A. Alsaui, M. Alawein, H. Fariborzi, 2019 Electron Devices Technol. Manuf. Conf. EDTM 2019 (2019) 371–373.
[210] Y. Telepinsky, V. Mor, M. Schultz, L. Klein, J. Appl. Phys. 111 (2012) 07C715.
[211] K. Olejník, V. Schuler, X. Marti, V. Novák, Z. Kašpar, P. Wadley, R.P. Campion, K.W. Edmonds, B.L. Gallagher, J. Garces, M. Baumgartner, P. Gambardella, T. Jungwirth, Nat. Commun. 8 (2017) 15434.
[212] L. Zhu, X. Xu, M. Wang, K. Meng, Y. Wu, J. Chen, J. Miao, Y. Jiang, Appl. Phys. Lett. 117 (2020) 112401.
[213] P. Wadley, B. Howells, J. Železný, C. Andrews, V. Hills, R.P. Campion, V. Novák, K. Olejník, F. Maccherozzi, S.S. Dhesi, S.Y. Martin, T. Wagner, J. Wunderlich, F. Freimuth, Y. Mokrousov, J. Kuneš, J.S. Chauhan, M.J. Grzybowski, A.W. Rushforth, K. Edmond, B.L. Gallagher, T. Jungwirth, Science (80-.). 351 (2016) 587–590.
[214] C.O. Avci, M. Mann, A.J. Tan, P. Gambardella, G.S.D. Beach, Appl. Phys. Lett. 110 (2017) 203506.
[215] X. Zhao, J. Wen, B. Yang, H. Zhu, Q. Cao, D. Wang, Z. Qian, Y. Du, ACS Appl. Mater. Interfaces 9 (2017) 36038–36044.

[216] Y. Zhang, W. Cai, W. Kang, J. Yang, E. Deng, Y.G. Zhang, W. Zhao, D. Ravelosona, IEEE Electron Device Lett. 39 (2018) 684–687.

[217] S. Das, A. Zaig, M. Schultz, L. Klein, Appl. Phys. Lett. 116 (2020) 262405.

[218] T. Devolder, J. Von Kim, F. Garcia-Sanchez, J. Swerts, W. Kim, S. Couet, G. Kar, A. Furnemont, Phys. Rev. B 93 (2016) 024420.

[219] B. Chen, T. Zhou, S.Y. Sim, S. Ter Lim, H. Gong, Phys. Lett. A 382 (2018) 3429–3434.

[220] J.M. Lee, C. Jang, B.C. Min, S.W. Lee, K.J. Lee, J. Chang, Nano Lett. 16 (2016) 62–67.

[221] R.A. Khan, P.M. Shepley, A. Hrabec, A.W.J. Wells, B. Ocker, C.H. Marrows, T.A. Moore, Appl. Phys. Lett. 109 (2016) 132404.

[222] Z.A. Bekele, X. Lan, K. Meng, X. Liu, J. Appl. Phys. 127 (2020) 113902.

[223] H. Yang, A. Thiaville, S. Rohart, A. Fert, M. Chshiev, Phys. Rev. Lett. 115 (2015) 267210.

[224] D.S. Han, N.H. Kim, J.S. Kim, Y. Yin, J.W. Koo, J. Cho, S. Lee, M. Kläui, H.J.M. Swagten, B. Koopmans, C.Y. You, Nano Lett. 16 (2016) 4438–4446.

[225] H. Yang, O. Boulle, V. Cros, A. Fert, M. Chshiev, Sci. Rep. 8 (2018) 12356.

[226] X. Ma, G. Yu, S.A. Razavi, S.S. Sasaki, X. Li, K. Hao, S.H. Tolbert, K.L. Wang, X. Li, Phys. Rev. Lett. 119 (2017) 027202.

[227] A. Giordano, R. Verba, R. Zivieri, A. Laudani, V. Puliafito, G. Gubbiotti, R. Tomasello, G. Siracusano, B. Azzerboni, M. Carpentieri, A. Slavin, G. Finocchio, Sci. Rep. 6 (2016) 36020.

[228] H.T. Nembach, J.M. Shaw, M. Weiler, E. Jué, T.J. Silva, Nat. Phys. 11 (2015) 825–829.

[229] X. Zhang, W. Cai, M. Wang, B. Pan, K. Cao, M. Guo, T. Zhang, H. Cheng, S. Li, D. Zhu, L. Wang, F. Shi, J. Du, W. Zhao, Adv. Sci. 8 (2021) 2004645.

[230] H. Lv, J. Fidalgo, A. V. Silva, D.C. Leitao, T. Kampfe, J. Langer, J. Wrona, B. Ocker, P.P. Freitas, S. Cardoso, Adv. Electron. Mater. 7 (2021) 2000976.

[231] Y.C. Lau, D. Betto, K. Rode, J.M.D. Coey, P. Stamenov, Nat. Nanotechnol. 11 (2016) 758–762.

[232] K. Garello, I.M. Miron, C.O. Avci, F. Freimuth, Y. Mokrousov, S. Blügel, S. Auffret, O. Boulle, G. Gaudin, P. Gambardella, Nat. Nanotechnol. 8 (2013) 587–593.

[233] J.Y. Chen, M. Dc, D. Zhang, Z. Zhao, M. Li, J.P. Wang, Appl. Phys. Lett. 111 (2017) 012402.

[234] J. Lourembam, L. Huang, B. Chen, J. Qiu, H.J. Chung, S.L.K. Yap, Q.J. Yap, S.K. Wong, S. Ter Lim, Adv. Electron. Mater. 7 (2021) 2001133.

[235] Z. Li, Y. Shi, K. Chi, W. Zhang, X. Feng, Y. Xing, H. Meng, B. Liu, Appl. Phys. Lett. 118 (2021) 132402.

[236] B. Chen, J. Lourembam, S. Goolaup, S. Ter Lim, Appl. Phys. Lett. 114 (2019) 022401.

[237] B. Chen, J. Lourembam, H.J. Chung, S. Ter Lim, J. Appl. Phys. 129 (2021) 163901.

[238] B. Dieny, I.L. Prejbeanu, K. Garello, P. Gambardella, P. Freitas, R. Lehndorff, W. Raberg, U.

Ebels, S.O. Demokritov, J. Akerman, A. Deac, P. Pirro, C. Adelmann, A. Anane, A. V. Chumak, A. Hirohata, S. Mangin, S.O. Valenzuela, M.C. Onbaşlı, M. d'Aquino, G. Prenat, G. Finocchio, L. Lopez-Diaz, R. Chantrell, O. Chubykalo-Fesenko, P. Bortolotti, Nat. Electron. 3 (2020) 446–459.

[239] G. Finocchio, M. Di Ventra, K.Y. Camsari, K. Everschor-Sitte, P.K. Amiri, Z. Zeng, J. Magn. Magn. Mater. 521 (2021) 167506.

[240] Q. Shao, P. Li, L. Liu, H. Yang, S. Fukami, A. Razavi, H. Wu, K. Wang, F. Freimuth, Y. Mokrousov, M.D. Stiles, S. Emori, A. Hoffmann, J. Akerman, K. Roy, J.-P. Wang, S.-H. Yang, K. Garello, W. Zhang, IEEE Trans. Magn. 57 (2021) 9427163.

[241] D.I. Albertsson, M. Zahedinejad, A. Houshang, R. Khymyn, J. Åkerman, A. Rusu, Appl. Phys. Lett. 118 (2021) 112404.

[242] M. Riou, F.A. Araujo, J. Torrejon, S. Tsunegi, G. Khalsa, D. Querlioz, P. Bortolotti, V. Cros, K. Yakushiji, A. Fukushima, H. Kubota, S. Yuasa, M.D. Stiles, J. Grollier, in: 2017 {IEEE} Int. Electron Devices Meet., IEEE, 2017.

[243] M. Romera, P. Talatchian, S. Tsunegi, F. Abreu Araujo, V. Cros, P. Bortolotti, J. Trastoy, K. Yakushiji, A. Fukushima, H. Kubota, S. Yuasa, M. Ernoult, D. Vodenicarevic, T. Hirtzlin, N. Locatelli, D. Querlioz, J. Grollier, Nature 563 (2018) 230–234.

[244] L. Rong-Hua, L. Li-Yuan, C. Li-Na, Z. Kai-Yuan, D. You-Wei, Prog. Phys. 40 (2020) 189.

[245] M. Zahedinejad, H. Fulara, R. Khymyn, A. Houshang, M. Dvornik, S. Fukami, S. Kanai, H. Ohno, J. Åkerman, Nat. Mater. 21 (2021) 81–87.

[246] X. Chen, W. Kang, D. Zhu, X. Zhang, N. Lei, Y. Zhang, Y. Zhou, W. Zhao, Nanoscale 10 (2018) 6139–6146.

[247] Q. Yang, R. Mishra, Y. Cen, G. Shi, R. Sharma, X. Fong, H. Yang, Nano Lett. (2022).

[248] M.A. Azam, D. Bhattacharya, D. Querlioz, J. Atulasimha, J. Appl. Phys. 124 (2018) 155122.

[249] P. Wadley, B. Howells, J. Železný, C. Andrews, V. Hills, R.P. Campion, V. Novák, K. Olejn\'\ik, F. Maccherozzi, S.S. Dhesi, S.Y. Martin, T. Wagner, J. Wunderlich, F. Freimuth, Y. Mokrousov, J. Kuneš, J.S. Chauhan, M.J. Grzybowski, A.W. Rushforth, K.W. Edmonds, B.L. Gallagher, T. Jungwirth, Science (80-.). 351 (2016) 587–590.

[250] M. Liu, J. Lou, S. Li, N.X. Sun, Adv. Funct. Mater. 21 (2011) 2593–2598.

[251] K.M. Song, J.S. Jeong, B. Pan, X. Zhang, J. Xia, S. Cha, T.E. Park, K. Kim, S. Finizio, J. Raabe, J. Chang, Y. Zhou, W. Zhao, W. Kang, H. Ju, S. Woo, Nat. Electron. 3 (2020) 148–155.

[252] B. Pan, D. Zhang, X. Zhang, H. Wang, J. Bai, J. Yang, Y. Zhang, W. Kang, W. Zhao, IEEE J. Electron Devices Soc. 7 (2019) 529–533.

[253] T. Bhattacharya, S. Li, Y. Huang, W. Kang, W. Zhao, M. Suri, IEEE Access 7 (2019) 5034–5044.

[254] Y. Yao, X. Chen, W. Kang, Y. Zhang, W. Zhao, IEEE Trans. Electron Devices 67 (2020) 2553–

2558.
[255] J. Zázvorka, F. Jakobs, D. Heinze, N. Keil, S. Kromin, S. Jaiswal, K. Litzius, G. Jakob, P. Virnau, D. Pinna, K. Everschor-Sitte, L. Rózsa, A. Donges, U. Nowak, M. Kläui, Nat. Nanotechnol. 14 (2019) 658–661.
[256] S. Li, W. Kang, X. Zhang, T. Nie, Y. Zhou, K.L. Wang, W. Zhao, Mater. Horizons 8 (2021) 854–868.
[257] T. Jin, F. Tan, W.C. Law, W. Gan, I. Soldatov, R. Schäfer, C. Ma, X. Liu, W.S. Lew, S.N. Piramanayagam, J. Magn. Magn. Mater. 475 (2019) 70–75.
[258] W.L.W. Mah, D. Kumar, T. Jin, S.N. Piramanayagam, J. Magn. Magn. Mater. 537 (2021) 168131.
[259] B. Yin, F. Corradi, S.M. Bohté, Nat. Mach. Intell. 3 (2021) 905–913.
[260] G. Srinivasan, A. Sengupta, K. Roy, Proc. 2017 Des. Autom. Test Eur. DATE 2017 (2017) 530–535.
[261] M.-H. Wu, M.-S. Huang, Z. Zhu, F.-X. Liang, M.-C. Hong, J. Deng, J.-H. Wei, S.-S. Sheu, C.-Wu I, G. Liang, T.-H. Hou, in: 2020 IEEE Symp. VLSI Technol., 2020.
[262] D.J. Gauthier, E. Bollt, A. Griffith, W.A.S. Barbosa, Nat. Commun. 12 (2021) 5564.
[263] G. Bourianoff, D. Pinna, M. Sitte, K. Everschor-Sitte, {AIP} Adv. 8 (2018) 55602.
[264] J. Dudas, J. Grollier, D. Marković, (2022).
[265] W. Jiang, L. Chen, K. Zhou, L. Li, Q. Fu, Y. Du, R.H. Liu, Appl. Phys. Lett. 115 (2019) 192403.
[266] H. Nomura, T. Furuta, K. Tsujimoto, Y. Kuwabiraki, F. Peper, E. Tamura, S. Miwa, M. Goto, R. Nakatani, Y. Suzuki, Jpn. J. Appl. Phys. 58 (2019) 70901.
[267] D. Pinna, G. Bourianoff, K. Everschor-Sitte, Phys. Rev. Appl. 14 (2020) 54020.
[268] K.Y. Camsari, B.M. Sutton, S. Datta, Appl. Phys. Rev. 6 (2019) 011305.
[269] S. Chowdhury, S. Datta, K.Y. Camsari, in: 2019 IEEE Int. ELECTRON DEVICES Meet., 2019.
[270] W.A. Borders, A.Z. Pervaiz, S. Fukami, K.Y. Camsari, H. Ohno, S. Datta, Nature 573 (2019) 390–393.
[271] J. Kaiser, S. Datta, Appl. Phys. Lett. 119 (2021) 150503.
[272] A.Z. Pervaiz, L.A. Ghantasala, K.Y. Camsari, S. Datta, Sci. Rep. 7 (2017) 10994.
[273] B. Sutton, K.Y. Camsari, B. Behin-Aein, S. Datta, Sci. Rep. 7 (2017) 1–9.